

Turbulent Diffuse Molecular Media with Non-ideal Magnetohydrodynamics and Consistent Thermochemistry: Numerical Simulations and Dynamic Characteristics

NANNAN YUE,¹ LILE WANG,^{1,2} THOMAS BISBAS,³ DONGHUI QUAN,³ AND DI LI^{4,3}

¹*The Kavli Institute for Astronomy and Astrophysics, Peking University, Beijing 100871, China*

²*Department of Astronomy, School of Physics, Peking University, Beijing 100871, China*

³*Zhejiang Laboratory, Hangzhou 311121, China*

⁴*National Astronomical Observatories, Chinese Academy of Sciences, Beijing 100101, China*

ABSTRACT

Turbulent diffuse molecular clouds can exhibit complicated morphologies caused by the interactions among radiation, chemistry, fluids, and fields. We performed full 3D simulations for turbulent diffuse molecular interstellar media, featuring time-dependent non-equilibrium thermochemistry co-evolved with magnetohydrodynamics (MHD). Simulation results exhibit the relative abundances of key chemical species (e.g., C, CO, OH) vary by more than one order of magnitude for the “premature” epoch of chemical evolution ($t \lesssim 2 \times 10^5$ yr). Various simulations are also conducted to study the impacts of physical parameters. Non-ideal MHD effects are essential in shaping the behavior of gases, and strong magnetic fields ($\sim 10 \mu\text{G}$) tend to inhibit vigorous compressions and thus reduce the fraction of warm gases ($T \gtrsim 10^2$ K). Thermodynamical and chemical conditions of the gas are sensitive to modulation by dynamic conditions, especially the energy injection by turbulence. Chemical features, including ionization (cosmic ray and diffuse interstellar radiation), would not directly affect the turbulence power spectra. Nonetheless, their effects are prominent in the distribution profiles of temperatures and gas densities. Comprehensive observations are necessary and useful to eliminate the degeneracies of physical parameters and constrain the properties of diffuse molecular clouds with confidence.

Keywords: Interstellar medium(847), Molecular clouds(1072), Astrochemistry(75), Hydrodynamical simulations(767), Magnetohydrodynamical simulations(1966)

1. INTRODUCTION

Molecular clouds are an essential phase of the interstellar medium (ISM), whose diffuse phase consists mainly of relatively dense ($\gtrsim 10^2 \text{ cm}^{-3}$), cool ($\lesssim 10^2$ K), and predominantly molecular gases (Draine 2011). Prominent morphological features, including filaments, bundles, cloud cores, and occasionally star-induced bubbles, are shaped by the turbulent fluid motions interacting with magnetic fields and radiation in these clouds (McKee & Ostriker 2007; Hennebelle & Falgarone 2012). Understanding the characteristics and evolution tracks of the diffuse molecular clouds is crucial for complete and comprehensive physical pictures of the evolution of the ISM in general. The diffuse

regions with densities $\rho \lesssim 10^3 m_p \text{ cm}^{-3}$, which seem less relevant to subsequent star formation processes, also draw researchers’ attention by exhibiting relatively complicated thermochemical details, including excitation of ro-vibrational molecular species in these relatively cold (typically $T \lesssim 10^2$ K) regions indicated by existing and incoming observations (e.g. Nehmé et al. 2008; Goldsmith et al. 2010; Langer et al. 2010; Ingalls et al. 2011; Rice et al. 2018).

Multiple numerical studies have been conducted regarding interstellar molecular gas’s morphological and dynamical characteristics. Pioneered by, e.g., Mac Low et al. (1998); Mac Low (1999), a series of studies on molecular clouds using 3D hydrodynamic or magnetohydrodynamic (MHD) simulations have focused on the morphologies and statistical characteristics of decaying or quasi-steady turbulence structures. Plenty of simulation works have assumed isothermal equations of states, even some of them have adopted ray-tracing or diffusive

radiative transfer (Raskutti et al. 2016, 2017; Kim et al. 2018, 2019). Nonetheless, consistent cooling and heating processes are considered essential to the reaction rates and excitation states of molecules, as well as the dissipation conditions for the turbulence scaling laws (Neufeld et al. 1995; Jappsen et al. 2007; Glover & Jappsen 2007; Tilley & Balsara 2011; Qian et al. 2018; Whitworth & Jaffa 2018). Simulating the turbulent media with such global prescriptions, rather than real-time local calculations, risks obscuring the interactions between thermochemistry and dynamics, leading to potentially unreliable consequences in dynamics and observational predictions.

Another critical factor is the non-ideal MHD effects. The weak ionization in molecular clouds leads to finite tensorial conductivities, exhibiting deviations from the flux-freezing ideal MHD. The tensor field of these magnetic diffusivities depends on the spatial distributions of plasma temperatures, free electrons, positive ions, and charged dust particles. Because of the lack of detailed thermochemical information, most simulation works tend to prescribe, rather than calculate in real-time, a set of conductivity or diffusivity parameters (Downes & O’Sullivan 2009; Tilley & Balsara 2011; Jones & Downes 2011, 2012). Even in the star formation simulations, magnetic diffusivities play crucial roles, Wurster et al. (2016) adopted significantly simplified equilibrium chemistry for charge carriers and ignored thermodynamics. However, the complications in charge-related reactions (especially those involving molecules and dust grains) and radiation cooling still necessitate real-time non-equilibrium thermochemistry despite the high computational costs, as have been identified in multiple studies on protoplanetary disks and molecular clouds (Xu & Bai 2016; Wang et al. 2019; Clark et al. 2019).

In order to address these critical issues for better intrinsic consistency and predictability for observations, we adopt the GPU-accelerated co-evolving non-ideal MHD-thermochemistry system that has been used in simulating protoplanetary disks (e.g. Wang et al. 2019) and predicting exoplanetary atmosphere observations (Wang & Dai 2021). There are several recent simulation studies that are conceptually similar. Works by e.g. Wurster et al. (2019); Wurster & Rowan (2024) have delved into the use of magnetic diffusivity profiles derived from chemical equilibrium to investigate the formation of stellar cores and protostellar disks in relatively dense molecular environments. Their findings underscore the critical role of magnetic diffusivities in addressing the magnetic braking issue. Other studies, such as Franeck et al. (2018); Clark et al. (2019); Lupi et al.

(2021), have examined various facets of molecular gases through the lens of non-equilibrium chemistry, focusing on the evolution of observables and tracer species. However, these studies have not taken into account the non-ideal MHD effects. Our approach aims to bridge this gap by conducting a comprehensive series of calculations within a dynamically quasi-steady turbulent framework. We will employ consistent magnetic diffusivities that are grounded in more extensive, non-equilibrium thermochemical networks in realtime. This endeavor aims at providing a more thorough exploration covering the lifecycle of typical diffuse molecular ISM, which spans approximately $\gtrsim 10^6$ yr. Our goal is to reflect the long-term evolution of thermochemical processes, thereby offering a more nuanced and accurate representation of the ISM’s behavior over extended periods. We will portray diffuse molecular clouds from diverse physical perspectives and systematically explore the space spanned by key physical parameters, especially the interstellar radiation field (ISRF), the cosmic rate (CR) ionization rate, the mean-field magnetic intensity, the specific dust cross-section, metallicity, and the turbulence energy injection rate. With detailed real-time thermochemical networks evolved and recorded, extended explorations on the observables and characterizations can also stem from these simulations in subsequent future works.

This paper is structured as follows. Section 2 briefly introduces the methods used in the simulations and describes the setups of several representative simulations. Setups and results of the fiducial simulation are elaborated in Section 3, and various models over the physical parameter space are explored in Section 4. We discuss the possible future explorations based on current results and conclude the paper in Section 5.

2. METHODS AND SETUPS

The computational schemes summarized in this section are primarily similar to Wang et al. (2019), with modifications particular to molecular clouds. We will also discuss the setups of numerical models in this paper.

2.1. Non-ideal Magnetohydrodynamics

The ionization of interstellar media, including the diffuse molecular gas explored in this paper, is always significantly non-zero. This fact makes their morphologies, evolution tracks, and thermochemistry profiles susceptible to different interactions between fluids and fields. We use the grid-based higher-order Godunov MHD code **Athena++** (Stone et al. 2020) on uniform Cartesian grids, with HLLD approximate Riemann solver and piecewise linear method (PLM) reconstruction. The MHD equa-

tions are solved in the conservative form:

$$\begin{aligned} \partial_t \rho + \nabla \cdot (\rho \mathbf{v}) &= 0 ; \\ \partial_t (\rho \mathbf{v}) + \nabla \cdot \left(\rho \mathbf{v} \mathbf{v} - \frac{\mathbf{B} \mathbf{B}}{4\pi} + P_{\text{tot}} \mathbf{I} \right) &= -\nabla \Phi ; \\ \partial_t \mathbf{B} &= \nabla \times (\mathbf{v} \times \mathbf{B} - c \mathbf{E}') ; \\ \partial_t \epsilon + \nabla \cdot \left[(\epsilon + P_{\text{tot}}) \mathbf{v} - \frac{(\mathbf{B} \cdot \mathbf{v}) \mathbf{B}}{4\pi} \right] &= S , \end{aligned} \quad (1)$$

where ρ , \mathbf{v} and p are the gas density, velocity and gas thermal pressure respectively, \mathbf{B} is the magnetic field, $P_{\text{tot}} \equiv p + B^2/(8\pi)$ is the total pressure, Φ is the gravitational potential, \mathbf{I} is the identity tensor, and

$$\epsilon \equiv \frac{p}{\gamma - 1} + \rho \left(\frac{v^2}{2} + \Phi \right) + \frac{B^2}{8\pi} \quad (2)$$

is the total energy density. The extra source term S in the energy equation reflects non-adiabatic processes that affect gas energy, which is calculated separately from the MHD solver in an operator-splitting manner (see §2.2). The adiabatic index γ is evaluated based on the real-time chemical components in each simulation zone. Non-ideal MHD effects are also considered by including an electric field in the local rest frame of fluids,

$$\mathbf{E}' = \frac{4\pi}{c^2} (\eta_{\text{O}} \mathbf{J} + \eta_{\text{H}} \mathbf{J} \times \mathbf{b} + \eta_{\text{A}} \mathbf{J}_{\perp}) , \quad (3)$$

where $\mathbf{b} \equiv \mathbf{B}/B$ is a unit vector along the local direction of \mathbf{B} , $\mathbf{J} = c \nabla \times \mathbf{B}/4\pi$ is the current density, and $\mathbf{J}_{\perp} \equiv \mathbf{b} \times (\mathbf{J} \times \mathbf{b})$ is the component of \mathbf{J} perpendicular to the local magnetic field. Different diffusivity components, including Ohmic (η_{O}), ambipolar (η_{A}), and Hall (η_{H}), are calculated for each simulated zone with the thermochemical conditions also elaborated in §2.2.

2.2. Non-equilibrium Thermochemistry with Consistency

The thermochemical processes significantly modulate the dynamic properties in turbulent molecular zones, which are also important in observational measurements and diagnostics. Technically, a “flow reaction” paradigm is required, in which the MHD is in charge of advecting chemical species and manipulating internal energy around the simulated space. Thermochemical reaction networks are co-evolved with the MHD in every simulation zone.

The advection of chemicals with MHD is accomplished by specific methods so that consistency of chemical elements and species fluxes in every timestep of MHD evolution is ensured. The advected chemical abundances and internal energy are then lead to the thermochemical solver for the current step, solving the following coupled

set of ordinary differential equations (ODEs) (in which the Einstein summation convention applies):

$$\frac{dn^i}{dt} = \mathcal{A}^i_{jk} n^j n^k + \mathcal{B}^i_j n^j ; \quad \frac{d\epsilon}{dt} = \Gamma - \Lambda ; \quad (4)$$

in which the terms $\{\mathcal{A}^i_{jk}\}$ describe two-body reactions, those in $\{\mathcal{B}^i_j\}$ represent photoionization, photodissociation, and spontaneous decays, and Γ and Λ represent all non-adiabatic heating, cooling, and heat transfer rates per unit volume, respectively. We use a multi-step implicit method with error control to solve since the ODEs (4) are usually stiff. The costs of co-evolving a stiff network in each zone throughout the domain at every timestep could be excessively high. For instance, a 3D simulation domain with 128^3 zones has to co-evolve $\sim 2 \times 10^6$ stiff systems in each step. In order to finish the simulations within reasonable “wall-clock time”, we use the thermochemistry solver implemented on graphic processing units (GPUs) to accelerate the simulations considerably for reasonable computing costs (see also Wang & Goodman 2017; Wang et al. 2019).

The set of chemical species, reactions, and thermodynamic processes largely follows Wang et al. (2019), with updates specific to diffuse molecular zones. The 23 species are: e^- (free electrons), H^+ , H , H_2 , H_2^+ , He , He^+ , O , O^+ , OH , H_2O , H_2O^+ , H_3O^+ , C , C^+ , CO , HCO^+ , CH , CH_2^+ , Gr , Gr^+ , Gr^- . Here Gr and Gr^{\pm} denote neutral and singly-charged dust grains, respectively. This set covers the most concerned chemical species in astronomical measurements. Internal energy density is also added as the last “species” to the set, and the temperature dependences of $\{\mathcal{A}^i_{jk}\}$ and $\{\mathcal{B}^i_j\}$ coefficients are converted to internal energy dependences (via proper heat capacities) for consistent thermochemical co-evolution. These “species” interact with each other through a network with 146 chemical reactions and thermodynamic processes (cooling and heating), most of which are included in the UMIST database (McElroy et al. 2013), and other necessary processes are also involved. To name a few mechanisms that are potentially important to the diffuse molecular cloud evolution, we have:

- Photoionizations by the interstellar radiation field (ISRF) and chemical species, including the photoionization of C, and photoelectric effects of dust grains.
- The ISRF photodissociation of multiple molecular species, e.g., OH, H_2O , CO, and H_2 .
- Cosmic ray (CR) ionization of multiple neutral species, especially H_2 , H, He, and O.

- Formation of important tracer molecules such as CO and OH, as subsequent products of ISRF photoionized C⁺, and CR ionized O⁺ (see also [Draine 2011](#)).
- Heating processes, including the energy injected via ISRF photoionization and dissociation, CR ionization, and the H₂ formation on the surfaces of dust grains (~ 1 eV per molecule formed).
- Radiative cooling processes, including rovibrational transitions of CO, OH, and H₂ ([Neufeld & Kaufman 1993](#); [Omukai et al. 2010](#)), and the fine structure transition of C⁺.

Note that the self-shielding effects for relevant photoionization and photodissociation processes are included with the recipes in [Heays et al. \(2017\)](#).

Both the radiation-related reactions and radiative cooling processes involve the penetration of photons, and column densities of different chemical species for photons to impinge and escape are the most important physical parameter. For the local structure simulations using periodic boundary conditions, the penetration columns for photons cannot be obtained consistently. Therefore, we estimate the column densities of species X involved in shielding is estimated by $N(X) \sim n(X)\bar{l}_v$, and the effective length l_v is approximated by

$$\bar{l}_v \sim \min\{l_v, l_{\text{cap}}\}; \quad l_v \equiv \frac{|\mathbf{v}|}{|\nabla \cdot \mathbf{v}|}, \quad (5)$$

where l_{cap} approximates the distance to the nearest source of radiation, describing case that the gas is largely uniform and static. There are also alternatives to this Sobolev estimation of effective length, e.g., $l_\rho \equiv \rho/|\nabla\rho|$ and $\bar{l}_\rho \sim \min\{l_\rho, l_{\text{cap}}\}$. However, the estimates based on velocity best emulates the physical mechanisms involved for the penetration of cooling and ionizing photons. For the diffuse region in the Taurus molecular cloud (TMC hereafter), we assume that $l_{\text{cap}} \sim 1$ pc represents the typical distance to one of the related radiation sources (e.g. young stars) in the nearby regions. In addition, the typical sizes of clumps inside the TMC diffuse regions are also considerably smaller than ~ 1 pc (see also [Goldsmith et al. 2010](#)), making $l_{\text{cap}} \sim 1$ pc a reasonably capping for the photon penetration length. We will revisit and confirm this assumption when analyzing the simulation results.

Similar to [Wang et al. \(2019\)](#), non-ideal MHD diffusivities are determined by the gas temperature and the charge carriers' abundances computed via the real-time non-equilibrium thermochemical network. The

general expressions for the three diffusivities read (e.g. [Bai 2011](#)),

$$\begin{aligned} \eta_{\text{O}} &= \frac{c^2}{4\pi} \left(\frac{1}{\sigma_{\text{O}}} \right), & \eta_{\text{H}} &= \frac{c^2}{4\pi} \left(\frac{\sigma_{\text{H}}}{\sigma_{\text{H}}^2 + \sigma_{\text{P}}^2} \right) \\ \eta_{\text{A}} &= \frac{c^2}{4\pi} \left(\frac{\sigma_{\text{P}}}{\sigma_{\text{H}}^2 + \sigma_{\text{P}}^2} \right) - \eta_{\text{O}}, \end{aligned} \quad (6)$$

where σ_{O} , σ_{H} and σ_{P} are Ohmic, Hall, and Pederson components of conductivity under magnetic fields, and

$$\begin{aligned} \sigma_{\text{O}} &= \frac{ec}{B} \sum_j n_j Z_j \beta_j, & \sigma_{\text{H}} &= \frac{ec}{B} \sum_j \frac{n_j Z_j}{1 + \beta_j^2}, \\ \sigma_{\text{P}} &= \frac{ec}{B} \sum_j \frac{n_j Z_j \beta_j}{1 + \beta_j^2}, \end{aligned} \quad (7)$$

in which $Z_j e$ is the charge and n_j the number density of the j^{th} charged species, and the Hall parameter β_j is the ratio of the gyrofrequency to the collision rate with neutrals,

$$\beta_j = \frac{Z_j e B}{m_j c} \frac{1}{\gamma_j}; \quad \gamma_j \equiv \frac{\langle \sigma v \rangle_j}{\langle m \rangle_n + m_j}, \quad (8)$$

where m_j is the charged species' molecular mass, $\langle m \rangle_n$ is the mean molecular mass of the neutrals, and $\langle \sigma v \rangle_j$ is the rate of collisional momentum transfer between the j^{th} species and the neutrals.

2.3. Turbulence Driving

From larger scales, turbulence energy cascades down to the simulated systems—a localized, periodic, cubic domain—in this work. Various methods have been adopted to emulate the injection of turbulence energy, and we adopt the mature methods adopted by [Mac Low \(1999\)](#). The perturbations are inserted as a globally uniform acceleration or inertial force. At each time step, a unity vector with random direction \hat{a} is assigned throughout the domain for the direction of perturbations. Assuming the amplitude of perturbation is A , the turbulence energy injection rate per by unit mass $\dot{\epsilon}_{\text{turb}}$ can be evaluated as,

$$\dot{\epsilon}_{\text{turb}} = A \left\{ [\langle \rho \rangle L_{\text{box}}^3]^{-1} \Delta t \sum_{\mathbf{i}} \delta V_{\mathbf{i}} \rho_{\mathbf{i}} \mathbf{v}_{\mathbf{i}} \cdot \hat{a} \right\}, \quad (9)$$

where L_{box} is the box length, $\langle \rho \rangle$ is the mean mass density throughout the domain, Δt is the current timestep, \mathbf{i} is the cell index, $\delta V_{\mathbf{i}}$, $\rho_{\mathbf{i}}$ and $\mathbf{v}_{\mathbf{i}}$ are the cell volume, mass density, and velocity vector for the \mathbf{i} -th cell, and the summation goes through all cells. In practice, we specify a fixed $\dot{\epsilon}_{\text{turb}}$ as one of the model parameters throughout the evolution period. In each time step, we use the

Table 1. Properties of the Fiducial Model (§2.4)

Item	Value
Geometries	
Simulation domain	$(0.04 \text{ pc})^3$
Resolution	$N^3 = 128^3$
Irradiation	
Interstellar radiation field (ISRF) †	$0.3 G_0$
Cosmic ray ionization *	$\zeta = 10^{-17} \text{ s}^{-1}$
Initial MHD Parameters	
Temperature	30 K
Density	$250 m_p \text{ cm}^{-3}$
Magnetic Field	$3 \mu\text{G}$
Initial abundances [n_X/n_H]	
H ₂	0.5
He	0.1
H	10^{-3}
e^-	10^{-6}
H ⁺	10^{-6}
O	3.2×10^{-4}
C	1.4×10^{-4}
Dust/PAH properties	
a_{Gr}	5 Å
σ_{Gr}/H	$\sim 10^{-23} \text{ cm}^2/H$

NOTE—†: G_0 denotes the Habing radiation flux (see also [Draine 2011](#)).

*: Total ionization rate per hydrogen atom by cosmic ray; the branching ratio of ionization is proportional to the elemental abundances (see e.g. [Bai & Goodman \(2009\)](#)).

summation in the braces of eq. (9) to determine the normalization factor A , calculate the perturbation acceleration vector $A\hat{a}$, inject kinetic energy into the system by $\mathbf{v}'_i = \mathbf{v}_i + A\hat{a}\Delta t$, and adjust the total energy density accordingly.

2.4. Simulation Setups

In brief, we carry out 3D MHD non-equilibrium thermochemical simulations in a $(0.04 \text{ pc})^3$ box with periodic boundary conditions. Non-equilibrium thermochemistry, whose network has 23 chemical species (plus internal energy density) and 146 reactions, is co-evolved in every zone of the MHD simulation. Non-ideal MHD effects with all components of tensorial conductivities are included.

For the diffuse region outside the boundary in the TMC, the ISRF UV photodissociation and photoionization parameter is $0.3 G_0$ ([Pineda et al. 2010](#)). At $t = 0$, we set the initial uniform mass density to be $\rho_{t=0} = 250 m_p \text{ cm}^{-3}$ with m_p the proton mass, and the initial temperature to be uniformly $T_{t=0} = 10 \text{ K}$

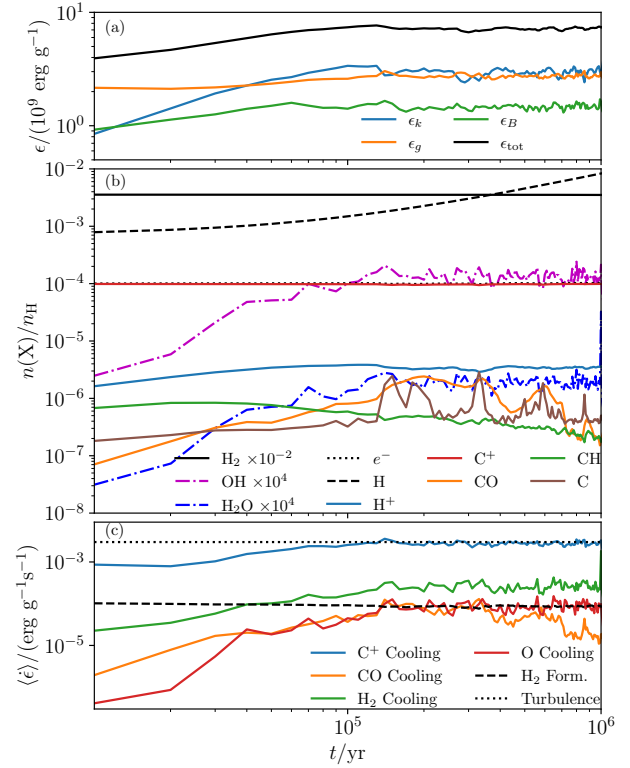


Figure 1. Time evolution of key physical parameters of the fiducial model. **Upper panel (a):** Domain-averaged specific energies (energy per unit mass; ϵ_k for the kinetic energy, ϵ_g for the gas internal energy, ϵ_B for magnetic energy, and ϵ_{tot} for the sum of all three components). **Middle panel (b):** Relative abundances of a few key chemical species throughout the simulation domain (note that the abundances of OH and H₂O are multiplied by 10^4). **Lower panel (c):** Average energy budgets per unit mass (solid lines for cooling, dash and dotted lines for heating or injections).

throughout the entire simulation domain. We also put a $\mathbf{B}_{t=0} = B_0 \mathbf{e}_x$ initial magnetic field, in which $B_0 = 3 \mu\text{G}$ for this fiducial model. We let the system evolve without additional energy input for 10^6 yr and examine the decay of the initial velocity perturbations and the gas cooling to select a time that best represents the thermochemical state of the TMC. These properties define the fiducial model, summarized in Table 1. Using these properties on hydrostatic models, we obtain two test cases that verify the applicability of our simulation system on molecular clouds. These tests, which also serve as the reference point of our subsequent analyses of thermochemistry for models *with* turbulences, are elaborated in Appendix A.

3. FIDUCIAL MODEL RESULTS

The evolution history of the fiducial model (Model 0) is illustrated in Figure 1. The dynamical evolution, char-

acterized by different components (internal energy ϵ_g , kinetic energy ϵ_k , and magnetic energy ϵ_B) of the specific energy, has mostly reached its quasi-steady state since $t \sim 10^5$ yr. After that, the energy balance only increases at a shallow rate ($\sim 10\%$ over $\sim 10^6$ yr). The thermochemistry evolution, nonetheless, has longer timescales. As the most important coolants for material in the diffuse molecular phase, variations in the abundances of a few key chemical species (e.g., CO, C, OH) fundamentally modulate the cooling channels in the thermodynamic budgets of the simulated gas. Overall, the comparison in timescales emphasizes the necessity of using non-equilibrium thermochemistry. In Figure 2 we confirm that the effective penetration length estimated by velocity divergences and density gradients yield results that are qualitatively consistent, which fall well below the capping length l_{cap} . The visual extinction is mostly negligible ($A_V < 0.5$ or even $\lesssim 0.1$) for $\gtrsim 99.5\%$ of the simulated zones, which is consistent with the studies for the diffuse regions TMC (e.g. Goldsmith et al. 2010). In addition, the Jeans length is significantly greater than the box scales even for compressed regions in the fiducial model. In addition, the virial parameter

$$\alpha_{\text{vir}} \sim \frac{v^2 + c_s^2}{G\rho l^2}, \quad (10)$$

are also large within the simulation domain. The median of α_{vir} reads $\langle \alpha_{\text{vir}} \rangle_{\text{median}} \sim 3$ with $l \sim l_J$ over the Jeans length, and $\langle \alpha_{\text{vir}} \rangle_{\text{median}} \sim 10^6$ over the typical clump scales estimated with $l \sim l_\rho$. These values indicate that the simulated diffuse regions are gravitationally unbound, and neglecting the self-gravity is eligible for the analyses on dynamics in this paper.

3.1. Fluid and Field Properties

As the initial fields was set uniformly $B_{x0} = 3 \mu\text{G}$, the corresponding initial plasma β was $\beta_0 = 1.23$. Turbulent evolution injects kinetic energy directly into the box, which subsequently branches into thermal energy by shocks, viscous dissipations, and magnetic energy via flux freezing. Similar to Figure 1, the evolution of kinetic energy spectrum and distribution functions (for $\lg T$ and $\lg \rho$) illustrated in Figure 3 reaches quasi-steady states after $t \gtrsim 10^5$ yr.

The kinetic energy spectrum does not show significant variation since $t \gtrsim 10^5$ yr, confirming that the quasi-steady state has already been reached. Magnetization for the fiducial model is intermediate ($\beta \sim 1$), with most of the gas dynamics being sub-Alfvénic (Figure 4) but supersonic (not shown in the figure). We observe a power law function damped at $k \sim 1.3 \times 10^3 \text{ pc}^{-1}$ (or equivalently $\sim 0.005 \text{ pc}$ spatial scale). At lower

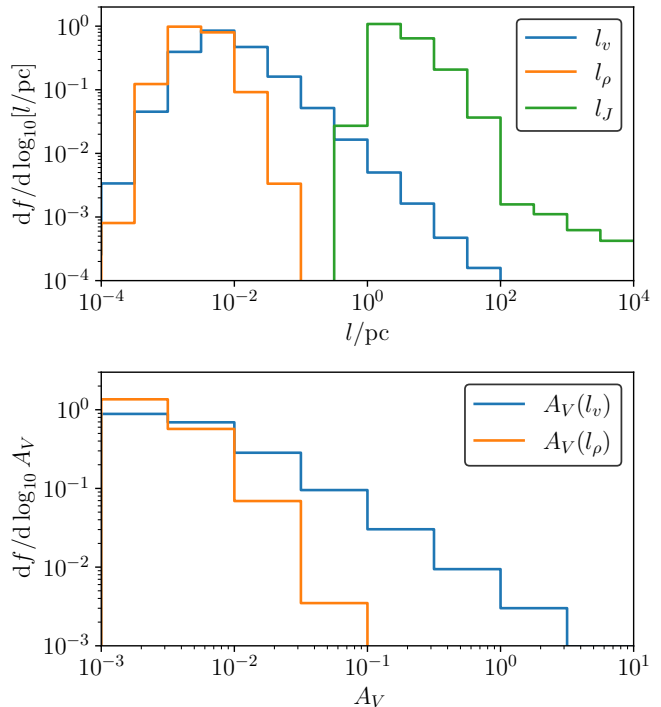


Figure 2. **Upper panel:** Distribution of volume fractions about the logarithm of scale lengths ($df/d \log_{10} l$), including extinction scale lengths estimated by velocity divergence (l_v), density gradient (l_ρ), and the Jeans length (l_J). **Lower panel:** Distribution of volume fractions about the logarithm of visual extinction, estimated by $A_V \sim N_{\text{H}}/(1.8 \times 10^{21} \text{ cm}^{-2})$ using l_v and l_ρ for the effective column densities, respectively.

wavenumbers down to $k \sim 0.4 \times 10^3 \text{ pc}^{-1}$ (larger scales at $\sim 1.5 \times 10^{-2} \text{ pc}$) the spectrum fits the Kolmogorov $E(k) \propto k^{-5/3}$ law. On a wider range of wavenumbers spanning roughly one decade (up to a damping scale $k \sim 1.5 \times 10^3 \text{ pc}^{-1}$), the energy power spectrum is comparable to the $E(k) \propto k^{-2}$ Burgers power law (for weakly magnetized compressible plasma with shocks, e.g., Kowal et al. 2007; Boldyrev & Perez 2009). The fitting over the $k/(10^3 \text{ pc}) \in [0.5, 1.5]$ range of wavenumbers prefers the k^{-2} power index ($\chi^2/N \sim 0.7$), and varying the wavenumber range included yields power index fittings roughly ranging from -1.9 through -2.1 . Compared to the fluid morphologies in the configuration space (Figure 4), the damping scale is close to the sizes of a typical eddy ($\sim 0.003 \text{ pc}$). These sizes are significantly greater than the numerical dissipation scale (roughly a few times the cell size, $\Delta x \simeq 3 \times 10^{-4} \text{ pc}$). Therefore, the dissipation should be physical rather than numerical or artificial. §4.1 re-examines such dissipation scales from the aspect of fields.

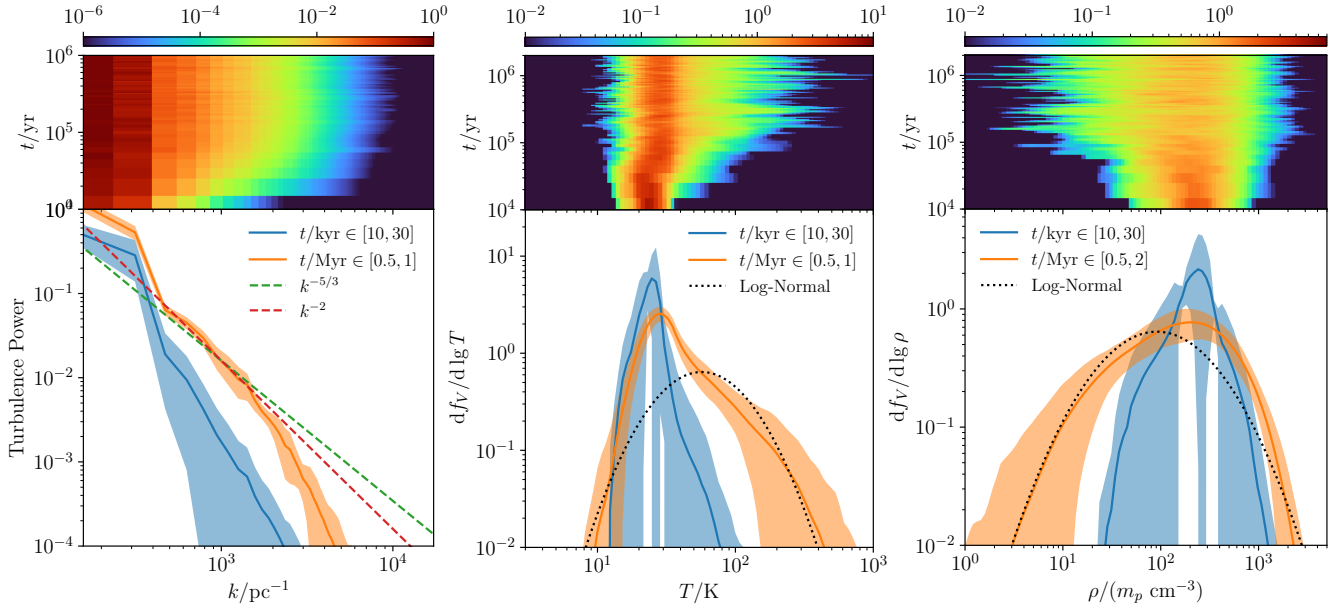


Figure 3. Turbulence kinetic energy power spectra for fiducial model. **Upper row:** Evolution of statistics over time; **Lower row:** Time-averaged statistics in different evolution epochs; shaded bands illustrate the ranges of 2σ variation. The left column shows the power spectra (whose lower panel compares them to the standard Kolmogorov $k^{-5/3}$ power law, and the k^{-2} power law), the middle column shows the distributions of spatial volume fraction f_V in the $\lg T$ space, and the right column shows the distributions in the $\lg \rho$ space. Dotted curves on the lower-middle and lower-right panels present the typical shapes of log-normal distributions for references.

The distribution functions of $\lg T$ and $\lg \rho$ exhibit more significant variations than the power spectrum. The upper branch of the $\lg T$ distribution and the lower branch of the $\lg \rho$ distribution mostly fit the log-normal distributions commonly observed in turbulences. In contrast, the other sides (low temperatures and high densities) consist of the peaks above the log-normal components that result directly from cooling processes. We notice $\gtrsim 10\%$ of the simulated domain (volume fraction) whose temperature is warm, $T > 10^2$ K. From the slices of the fiducial model in Figure 4, we notice that these relatively warm regions usually have lower (but not necessarily lowest) mass densities. Such temperatures will likely populate the ro-vibrational energy levels of a few vital molecular species. They may lead to important observational consequences, which will be discussed in our following paper.

Compared to the initial conditions of $B_0 = 3 \mu\text{G}$ and $\beta_0 = 1.23$, the evolved magnetic fields depicted in Figure 4 demonstrate a moderate enhancement due to turbulent dynamics, reaching magnitudes of approximately $\sim 5 - 10 \mu\text{G}$ predominantly in regions of compression characterized by relatively high density ($\rho \gtrsim 10^3 m_p \text{ cm}^{-3}$) and low temperature ($T \lesssim 20$ K). Areas where the plasma beta (β) is significantly less than unity typically exhibit magnetic field strengths close to the initial value of $|B| \sim B_0$. These regions are predominantly

composed of kinematically decelerated gas with densities lower than the initial density, ($\rho \lesssim 10^{-1} \rho_0$), and temperatures well above average ($T \sim 10^2$ K). The magnetization within these regions achieves a quasi-steady state, representing a balance between the amplification effects of turbulent motion and the counteracting influence of magnetic diffusion. The lower-right panel presents Re_p , the magnetic Reynolds number for the ambipolar (“Pederson”) component of magnetic diffusivities, defined as,

$$\text{Re}_p \equiv \frac{|\mathbf{v}| l_{\text{dyn}}}{\eta_p} \sim \frac{|\mathbf{v}|^2}{\eta_p |\nabla \cdot \mathbf{v}|}, \quad (11)$$

in which we have used the uncapped $l_v \equiv |\mathbf{v}|/|\nabla \cdot \mathbf{v}|$ to estimate the dynamical length scale l_{dyn} . The intensity of magnetic diffusion relative to the inertia becomes more important with smaller Re_p . From the figure, we observe a significant fraction of space where $\text{Re}_p \lesssim 10$ or even less than unity, indicating that the ambipolar diffusion becomes a major channel of dissipating the growths of fields through turbulences. These Re_p values emphasize the necessity of including non-ideal MHD effects, which can only be accurately modeled by the inclusion of real-time thermochemistry (see §2.1, §2.2).

3.2. Thermochemistry and Its Evolution

Profiles of chemical species vary in the simulation, from their abundances to their forming and destruction

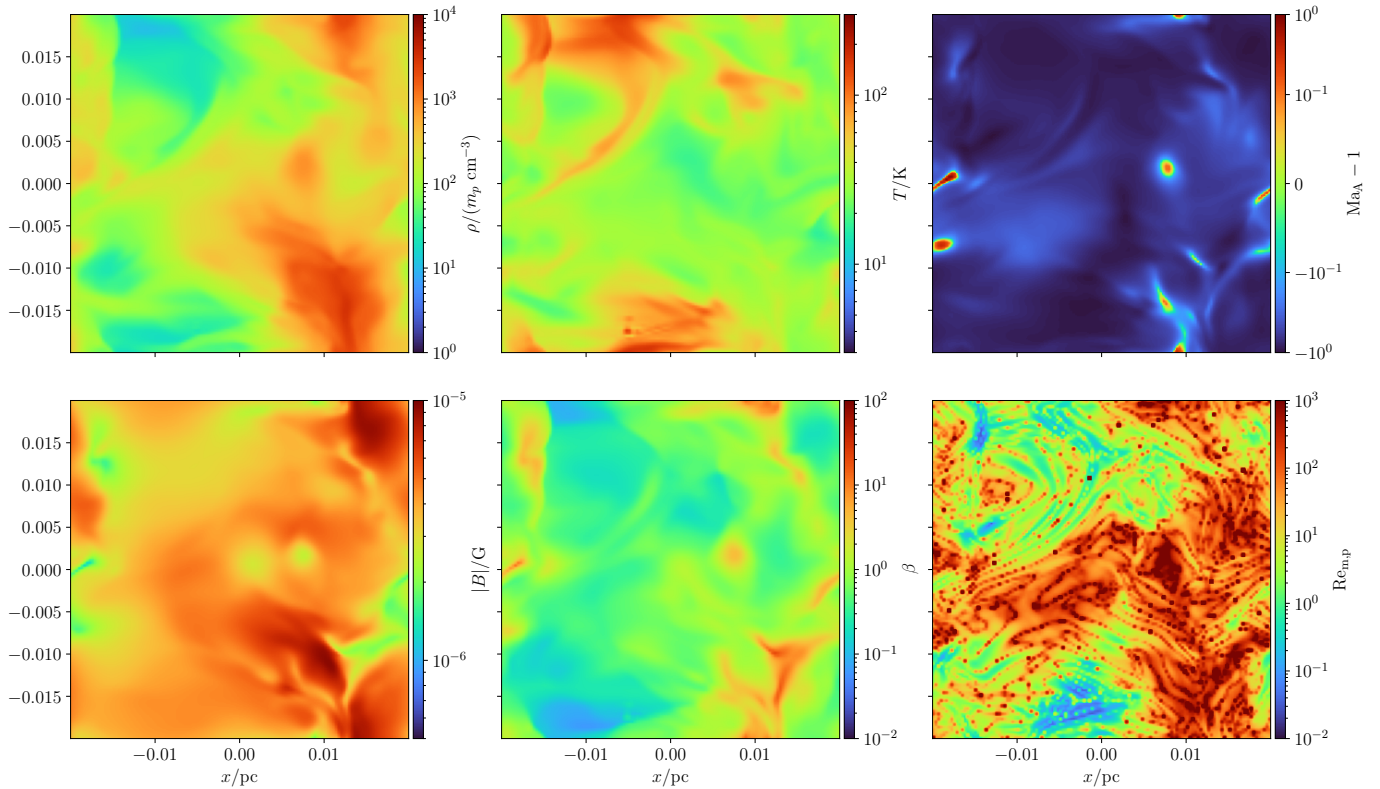


Figure 4. Slices of physical parameters at the $z = 0$ plane, illustrating the $t = 10^6$ yr snapshot for the fiducial model. The upper row shows the key hydrodynamical parameters (mass density ρ , temperature T , and $\text{Ma}_A - 1$ ($\text{Ma}_A \equiv |v|/[B/(4\pi\rho)]^{1/2}$) is the Alfvénic Mach number), and the lower row shows relevant field parameters (magnetic field strength $|B|$, plasma β parameter, and magnetic Reynolds number Re_p).

pathways. Molecular hydrogen H_2 are often traced by other molecules with relatively strong emission powers, e.g., CO, OH, and C^+ . In Figure 5, we present the abundances relative to hydrogen nuclei n_{H} of a few key chemical species in the $z = 0$ plane for the fiducial model at $t = 5 \times 10^4$ yr, 2×10^5 yr, and 10^6 yr, respectively.

3.2.1. Abundances of Molecules

The relative abundance of X_{CO} for CO, which is the most frequently adopted H_2 tracer, varies over time along the evolution track. Formation of CO is lead by the chain from C^+ to CH (e.g. [Draine 2011](#)), reaching its maximum around $t \sim 2 \times 10^5$ yr and starting to decline afterward (which can also be observed in Figure 5). Such decline comes from the increased abundance of atomic H competes with O in consuming CH, which is qualitatively similar to the tests in Appendix A (see also the evolving CH abundances in Figure 5). The timescale of overall X_{CO} variation is roughly $\tau_{X_{\text{CO}}} \gtrsim 2 \times 10^5$ yr. It is a reasonable assumption that diffuse molecular gas coexists with the overall molecular region, which may subsequently disperse due to intense photodissociation following the formation of nearby young stellar objects.

The timescale over which X_{CO} varies is on par with the lifespan of molecular regions in their entirety; therefore, this timescale merits close consideration when one intends to investigate the long-term chemical evolution of diffuse molecular gases.

We notice that the CO abundance is one order of magnitude above the hydrostatic tests (Appendix A and Figure 13). Because the formation of CH_2^+ , the rate-determining step in the reaction chain leading to CO, is primarily the two-body reaction $\text{C}^+ + \text{H}_2 \rightarrow \text{CH}_2^+$, the compression caused by shocks and subsonic motions in turbulences largely enhances the whole rate of formation. This enhancement also leads to the spatial variations in X_{CO} , as well as the stochasticity of $\langle X_{\text{CO}} \rangle$ even though the spatial average is taken across the domain. In Figure 6, one can observe that the most of CO molecules exist on the average temperature (~ 30 K) and relatively high density, exhibiting distribution contours similar to H_2 on the $\lg n - \lg T$ plane. When coming to the $\lg n - \lg n(\text{H}_2)$ plane, X_{CO} varies by about one decade at each n_{H_2} , and the median of n_{CO} increases faster than linear with greater n_{H_2} , which is another consequence of the two-body reaction nature of the

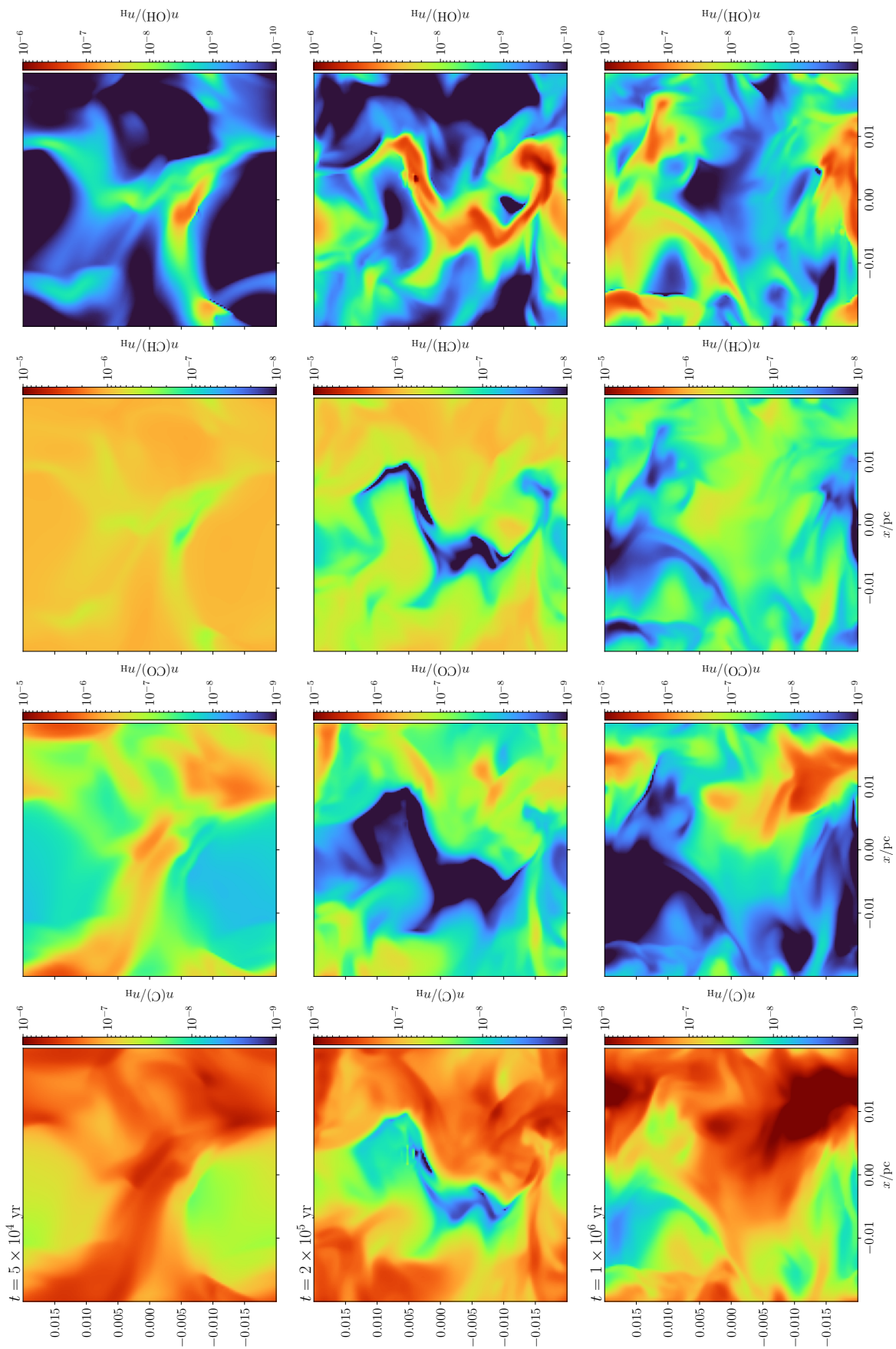


Figure 5. Slices at the $z = 0$ plane for the fiducial for different evolution time ($t = 5 \times 10^4$ yr for the upper row, and 5×10^5 yr for the lower row), showing the relative abundances of C (left column), CO (middle-left column), CH (middle-right column), and OH (right column), normalized to the total density of hydrogen nuclei n_{H} .

rate-determining step. Therefore, X_{CO} values should be carefully adopted with their temporal and spatial variations taken into account adequately when one wants to characterize diffuse molecular gases with reasonable accuracy. Similar conclusions about X_{CO} have emerged from various other simulation studies (e.g. Clark et al. 2019; Lupi et al. 2021). These studies emphasize the integration of co-evolved chemistry with magnetohydrodynamics (MHD) when analyzing chemical tracers within the molecular ISM. There are also extra complications at temperatures below the threshold of $T \lesssim 20$ K, CO molecules are prone to further condensation onto the surfaces of dust grains (Cazaux et al. 2017). Given that our study predominantly concentrates on the gas-phase characteristics of diffuse molecular regions, we have opted to exclude these additional complexities in the present paper. Instead, we intend to reserve more exhaustive explorations for future research endeavors that delve into multi-phase mechanisms, thereby providing a more comprehensive understanding of the interplay between gas and dust in these environments.

The OH molecules show contrasts to CO. Because of turbulence compressions, they are $\sim 10^4$ more abundant than the hydrostatic tests in Appendix A. Nonetheless, because e^- and atomic O compete for the crucial progenitors (H_2^+ and H_3^+), regions with high densities could not always gain more OH from increased two-body reaction rates. At higher temperatures, the reaction between e^- and H_x^+ ($x = 2, 3$) is slightly suppressed (rate coefficient $\propto T^{-0.5}$; see McElroy et al. 2013) while the channel with O leading to H_2O^+ and then OH is not affected. In addition, the charge exchange channel ($\text{H}^+ + \text{O} \rightarrow \text{O}^+ + \text{H}$) that has secondary importance in the formation of OH prefers higher temperatures and higher H^+ abundances, which mostly occur on the edges of high-density regions where gas compression is likely to happen. Therefore, the distribution of OH on the $\lg n - \lg T$ plane prefers the compressed regions with intermediately low temperature and densities, showing a “ridge”, roughly starts from the lower-left part (low n , low T) to the upper-right corner (Figure 6). On the $\lg n - \lg n(\text{H}_2)$ plane, the correlation between OH and H_2 is loose and should not be used alone to deduce the properties of H_2 .

3.2.2. Energy Dissipation

Dissipation of energy is crucial to the quasi-steady turbulent structures in the system. Short of cooling mechanisms, the fluids will eventually stop behaving turbulently after their total internal energy (ϵ_g) exceeds the amount of energy injection from the largest scales. Enumerating all prospectively important cooling processes in the simulation, we identify a few major cooling mech-

anisms in the fiducial model and present their corresponding heating and cooling timescale maps in the top and middle rows of Figure 7.

It is observed that cooling via the fine structure transitions of C^+ mainly appears at boundaries separating dense and diffuse regions, while the CO ro-vibrational transitions are responsible for cooling the dense gas. The rotational transitions of CO are characterized by lower energy separations. For instance, the transition $J = 1 \rightarrow 0$ corresponds to a wavelength of $\lambda = 2.6$ mm. This is in contrast to the fine structure transition of ionized carbon (C^+), particularly the $[\text{C II}]$ line at $\lambda = 158\mu\text{m}$ via which most of the C^+ cooling takes place. The distinction between these two cooling channels is more apparent at relatively low temperatures $T \lesssim 30$ K. This natural divergence at cooler regimes has been previously discussed by e.g. Richings et al. (2014a,b), who utilized thermochemical calculations in the absence of hydrodynamics or MHD. In the context of co-evolved non-ideal MHD, this phenomenon is further intertwined with the turbulence dynamics. The compression of gas through turbulence facilitates more efficient production of CO from C^+ through a sequence of chemical reactions. Concurrently, the increase in collisional partners augments the difference in cooling efficiency between CO and C^+ at low temperatures.

Due to relatively low temperature, the cooling mechanism on the third panel—the ro-vibrational transitions of CO—are $\sim 10^{-2}$ less efficient than C^+ and H_2 . The detectability of these transitions could lead to significant observational effects, which will be discussed in more detail in our following paper. In total, the evolution of multiple cooling mechanisms is compared to the energy injection mechanisms: (1) turbulent energy injection, and (2) the formation of H_2 on grain surfaces (each H_2 formed will introduce ~ 1 eV into the gas thermal energy; e.g. Pantaleone et al. 2021). The overall energy balance is close to equilibrium, yet with a small surplus on the heating side (around $\sim 10^{-4}$ erg g s $^{-1}$). Multiplying this surplus by $\sim 10^6$ yr explains the gradual increase in the total specific energy (Figure 1 a).

4. PARAMETER STUDIES: VARIOUS MODELS

As §3 discovered, various physical parameters are related to the behaviors in the simulated diffuse cloud. In order to examine their prospective influences, we conduct extra simulations examining the outcomes of modifying important physical parameters. Table 2 lists relevant models marked by different symbols; each varies only one parameter at a time.

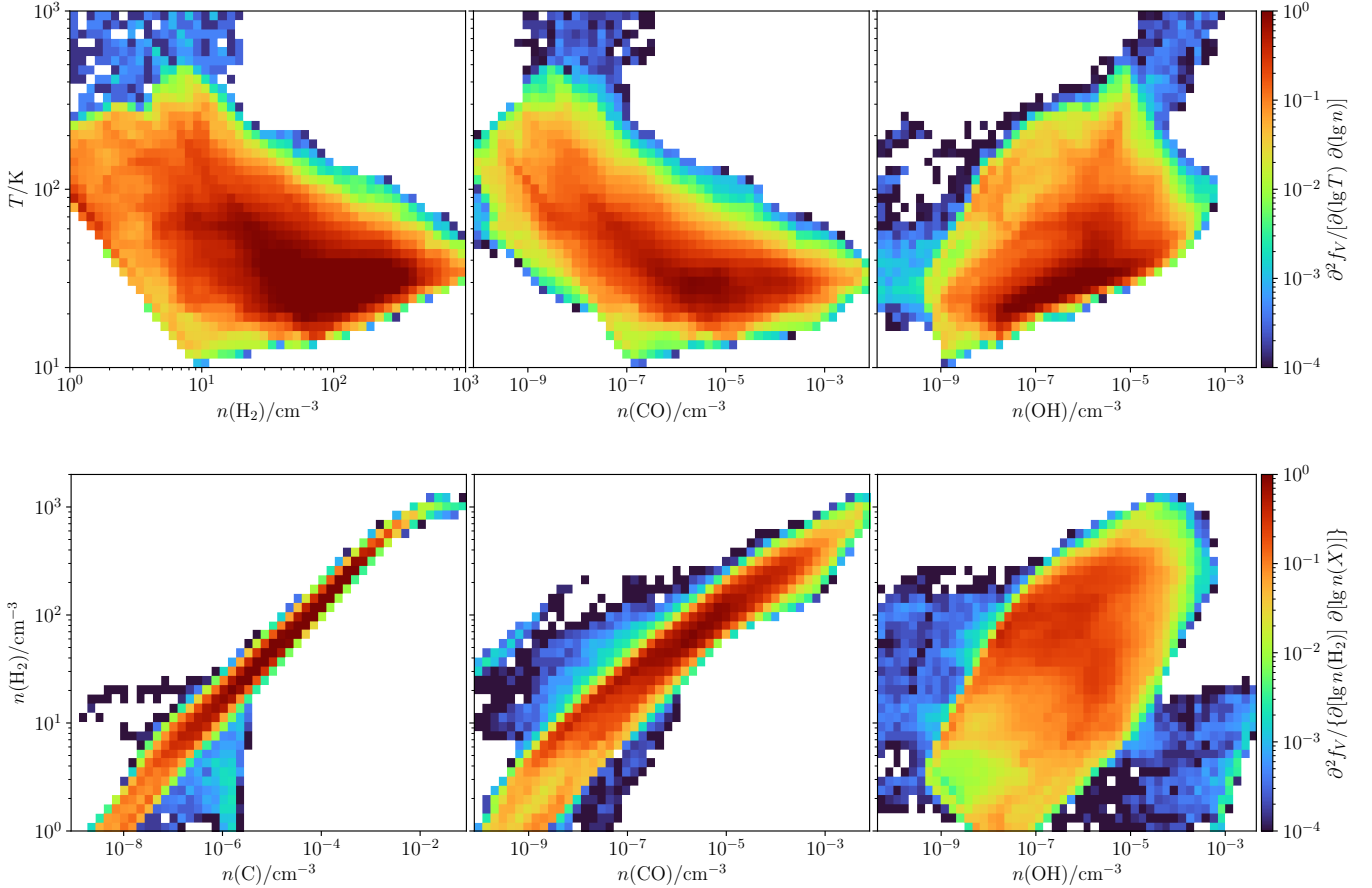


Figure 6. Distribution of spatial volume fraction f_V in the spaces spanned by $\{\lg T\} \times \{\lg n(X)\}$ (upper row) and $\{\lg n(\text{H}_2)\} \times \{\lg n(X)\}$ (lower row), where X stands for different chemical species indicated on each panel.

4.1. Fields and Fluids

Turbulences can amplify the fields by flux freezing. This process is dispersed and dissipated by the non-ideal MHD effects, and we confirm this point by comparing Model 0 and Model I (ideal MHD). Figure 8 illustrates the difference between these two models. Although the power spectra are identical at the spatial scales of energy injection (viz. lowest wavenumbers), the inertial range of Model I has greater kinetic power, ~ 3 times Model 0. The damping wavenumber of the fiducial Model 0 is also lower ($k \simeq 1.3 \times 10^3 \text{ pc}^{-1}$) compared to Model I ($k \simeq 2.2 \times 10^3 \text{ pc}^{-1}$), exhibiting the effects of magnetic diffusion that dissipates the kinetic energy at larger scales with greater efficiencies. The distribution function in the $\lg T$ space for Model I shows that a considerably smaller fraction of gas has temperatures above $\sim 10^2 \text{ K}$ compared to Model 0, which is attributed to the absence of non-ideal MHD heating, as well as the tighter fluid-field coupling that reduces the shocks and collisions. These differences confirm the importance of

including proper and consistent non-ideal MHD effects when simulating magnetized molecular clouds.

Coupling between fluids and fields has another side effect: the energy transfer to smaller scales is inhibited. Turbulent motions on smaller scales tend to amplify the fields more efficiently, causing higher branching ratios into magnetic energy. In the simulation series including Models B0 (a pure hydrodynamic simulation without any fields), fiducial, B1, and B10, the power spectra are very similar in the range $k \lesssim 1 \times 10^3 \text{ pc}^{-1}$. At the same time, the amplitudes at higher wavenumbers are anti-correlated to the initial field strengths. The situation of Model B10 is more severe than others, whose strong magnetic fields suppress the kinetic power by almost one decade and narrow the distribution functions in the $\lg T$ and $\lg \rho$ spaces. This phenomenon can constrain the upper limits of field intensities in observed molecular gases. For example, the average field strength is unlikely to be greater than $\sim 10 \mu\text{G}$ given the discovery of considerable fractions of $T \gtrsim 1.5 \times 10^2 \text{ K}$ warm regions. With the rotational transition of H_2 observed identifying gas temperature $T \gtrsim 200 \text{ K}$ in the diffuse molecular gas in

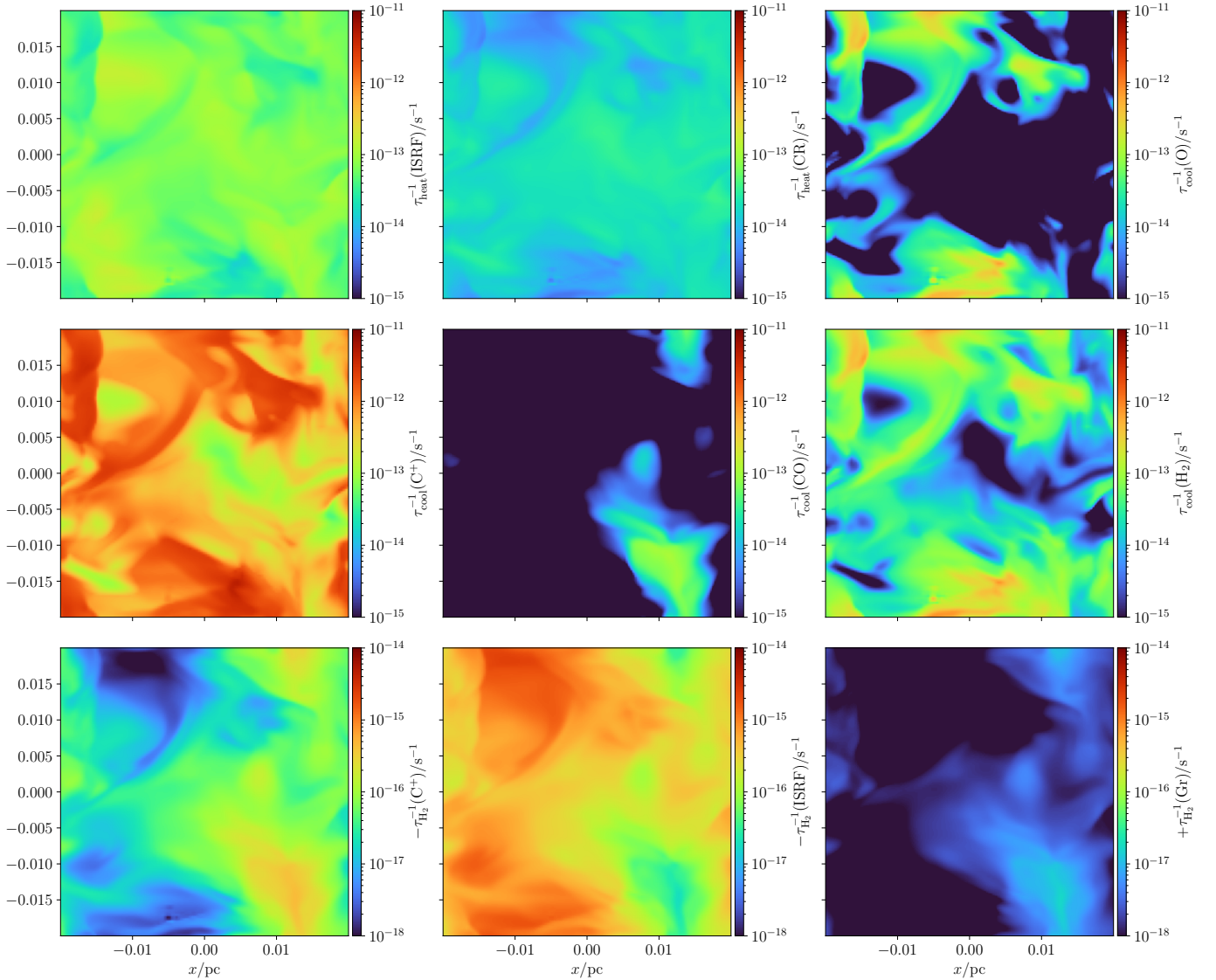


Figure 7. Important thermochemical rates, quantified as the reciprocals of timescales (τ^{-1}), illustrating the $z = 0$ plane for the fiducial model at the $t = 2 \times 10^6$ yr snapshot. **The top and middle rows** show the heating and cooling processes. The upper-left panel illustrates the heating via the ISRF dissociation and ionization, the upper-middle panel presents the heating by cosmic rays, and the rest panels are for cooling: the fine structure transitions of O (upper-right panel) and C^+ (middle-left panel), and the ro-vibrational transitions of CO (middle panel) and H_2 (middle-right panel). The cooling rates by OH are relatively tiny and thus omitted. **The bottom row** shows the rates related to H_2 number densities: the destruction rates via the reactions with C^+ (left panel) and photodissociation (middle panel), and the formation rates via the catalyzed reaction by dust grains (right panel).

the TMC region (e.g. Goldsmith et al. 2010), this result prospectively provide a constraint on the strength of magnetization therein.

Recent simulations have delved into the intricacies of magnetized molecular clouds, with notable studies such as that by Grete et al. (2021), which explored the suppression of kinetic energy cascade due to magnetic tension. This finding aligns well with the observed trends across a range of simulations. However, it is crucial to

acknowledge that the numerical diffusivities associated with both fluids and fields, which vary with spatial resolution in these simulations, may be interlinked with the identification of damping effects attributed to magnetic tension. For a thorough and quantitative examination of how small-scale structure growth is curtailed by magnetic fields, it is essential to ensure a consistent coupling between fields and fluids. This should be governed by appropriate magnetic diffusivities and should include a

Table 2. Physical parameters of various models (§4)

Model	Description	$\langle\epsilon\rangle/(10^9 \text{ erg g}^{-1})$			$\log_{10}[n(\text{X})/n_{\text{H}}]$				$\log_{10}[\langle\dot{\epsilon}\rangle_{\text{cool}}/(\text{erg g}^{-1} \text{ s}^{-1})]$			
		Thermal	Kinetic	Magnetic	e^-	C^+	CO	OH	C^+	CO	H_2	O
(1)	(2)	(3)	(4)	(5)	(6)	(7)	(8)	(9)	(10)	(11)	(12)	(13)
0	Fiducial model	2.8	3.0	1.5	-3.99	-4.01	-6.58	-7.87	-2.55	-4.73	-3.57	-4.05
I	Ideal MHD	2.7	3.2	1.9	-3.99	-4.01	-6.83	-7.84	-2.53	-4.90	-3.68	-4.29
B0	No magnetic fields	2.7	3.4	0.00	-3.99	-4.01	-6.61	-7.73	-2.55	-4.67	-3.57	-4.13
B1	$B_{x0} = 1 \mu\text{G}$	2.7	3.4	0.5	-4.00	-4.01	-6.33	-7.84	-2.57	-4.46	-3.52	-4.04
B10	$B_{x0} = 10 \mu\text{G}$	2.8	1.7	9.9	-3.99	-4.01	-6.52	-8.06	-2.54	-4.81	-3.77	-4.22
T4	$\dot{\epsilon}_{\text{turb}} = 3 \times 10^{-4} \text{ erg s}^{-1} \text{ g}^{-1}$	1.9	0.6	1.1	-3.98	-4.01	-7.05	-9.35	-3.35	-5.53	-4.91	-6.43
T2	$\dot{\epsilon}_{\text{turb}} = 3 \times 10^{-2} \text{ erg s}^{-1} \text{ g}^{-1}$	6.5	13.1	2.6	-4.02	-4.03	-6.45	-7.01	-1.77	-4.03	-1.99	-2.59
N4	$\rho_0 = 2.5 \times 10^4 m_p \text{ cm}^{-3}$	2.8	3.3	0.1	-6.21	-6.53	-4.36	-8.21	-3.93	-2.60	-3.35	-4.36
N6	$\rho_0 = 2.5 \times 10^6 m_p \text{ cm}^{-3}$	2.4	3.2	0.01	-8.10	-9.49	-4.40	-10.45	-6.53	-2.56	-3.59	-5.62
G0	$G = 0$	3.9	3.2	0.9	-5.36	-5.82	-4.56	-6.32	-3.29	-2.97	-3.02	-3.33
G3	$G = 3 G_0$	3.0	2.9	1.5	-3.98	-4.00	-8.79	-8.69	-2.45	-6.67	-3.52	-3.91
CR0	$\xi_{\text{CR}} = 0$	2.7	2.9	1.4	-4.02	-4.02	-5.94	-10.04	-2.57	-4.32	-3.59	-4.05
CR15	$\xi_{\text{CR}} = 10^{-15} \text{ s}^{-1}$	3.8	2.9	1.7	-3.53	-4.00	-7.48	-6.74	-2.11	-5.32	-3.27	-3.73
M01	$0.1 \times$ Fiducial metal	3.7	2.9	1.1	-4.65	-5.00	-8.46	-7.61	-2.69	-6.30	-2.99	-3.86
M10	$10 \times$ Fiducial metal	2.8	3.0	1.6	-3.44	-3.44	-5.93	-8.06	-2.55	-4.09	-3.62	-4.27

NOTE—(1)–(2): Model codes and descriptions; each model is different from the fiducial model by only one physical parameter.

(3)–(5) Average specific energy components (thermal $\langle\epsilon_g\rangle$, kinetic $\langle\epsilon_k\rangle$, and magnetic $\langle\epsilon_b\rangle$). Note that for a predominantly molecular gas, the specific energy components can be converted to temperature as $\langle T \rangle \simeq 11.4 \text{ K} [\langle\epsilon_g\rangle/(10^9 \text{ erg g}^{-1})]$, and root-mean-squared velocity $\langle v^2 \rangle^{1/2} \simeq 0.45 \text{ km s}^{-1} [\langle\epsilon_k\rangle/(10^9 \text{ erg g}^{-1})]^{1/2}$. The average plasma β can also be estimated by $\langle\beta\rangle \simeq \langle\epsilon_g\rangle/\langle\epsilon_b\rangle$.

(6)–(9): Logarithms of relative abundances of key chemical species.

(10)–(13): Specific cooling rates (energy loss rate per unit mass) via different coolants.

consistent approach to the ultimate dissipation of energy through thermodynamic processes. In the current work, the suppression of energy cascade by field tensions is observed to influence the power spectra at higher magnetic field strengths. The threshold for this effect is distinctly identifiable between magnetic field strengths of $B_0 = 3 \mu\text{G}$ and $10 \mu\text{G}$. Below this threshold, the damping of fluid fluctuations predominantly occurs through non-ideal MHD dissipation mechanisms. This can be inferred by comparing the damping wavenumbers across Models B3, B10, 0 (Fiducial), and I (ideal MHD).

Higher average mass density yields large plasma β , lowering the relative significance of magnetic pressure and stresses. As a result, Models N4 and N6 show very similar power spectra, which have considerably greater amplitudes compared to the fiducial Model 0 (see Figure 10)—these spectra are also very similar to the field-free Model B0. As the cooling rates are roughly proportional to the square of mass density at a fixed temperature, while the turbulence energy injection rate per unit volume is proportional to the mass density itself (given fixed $\dot{\epsilon}_{\text{turb}}$ per unit mass), the temperature distributions

of Models N4 and N6 appear on the lower end compared to Model 0.

Another important process affected by the average density is the recombination of ions. As the recombination rate coefficients are mostly the functions of temperatures, assuming that the temperature is roughly fixed and that there is only one ionizable species ($\text{X} \leftrightarrow e^- + \text{X}^+$) thus $n_e = n(\text{X}^+)$, the ionization–recombination balance roughly reads,

$$\alpha x_e^2 n_{\text{H}}^2 \sim \zeta n_{\text{H}} \Rightarrow x_e \sim n_{\text{H}}^{-1/2}, \quad n_e \equiv x_e n_{\text{H}} \sim n_{\text{H}}^{1/2}. \quad (12)$$

In the series consisting of Models 0, N4, and N6, the fraction x_e drops faster than $\rho^{-1/2}$. The main charge carrier in Model N4 before $t \sim 2 \times 10^5 \text{ yr}$ is still C^+ , and changes to H^+ afterward due to efficient formation of CO that uses up almost all carbon. Model N6 also has H^+ as the main charge carrier, but from a different origin: its self-shielding and cross-shielding for the ISRF ionization of neutral C is significant that the dominating ionization process is the cosmic ray ionization of H_2 in the first place. Without efficient CO formation, the specific energy keeps growing until $\sim 10^5 \text{ yr}$, after which $\langle X_{\text{CO}} \rangle$ exceeds $\sim 10^{-5}$, and the subsequent cool-

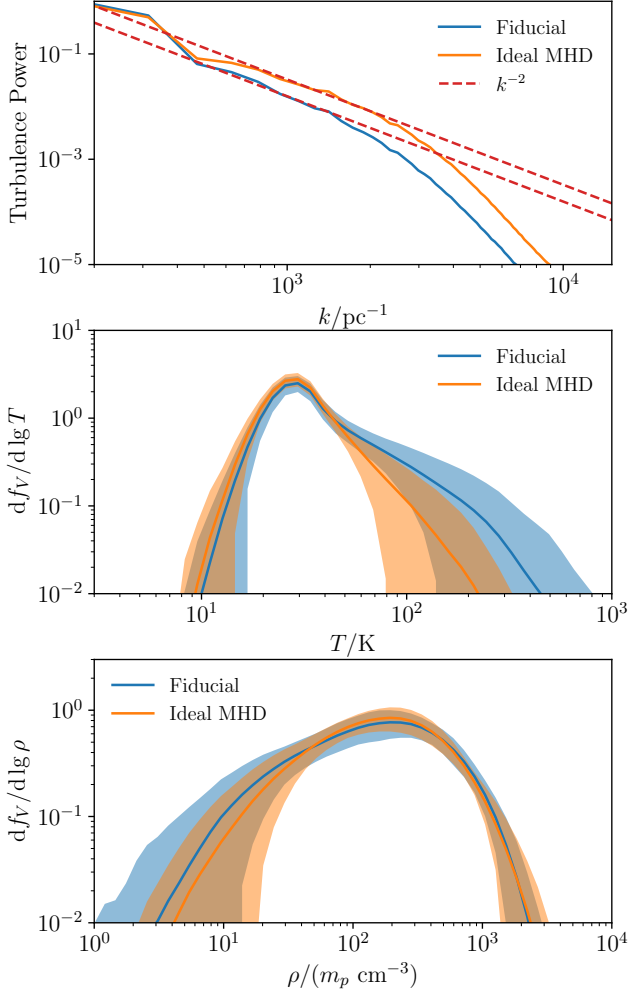


Figure 8. Statistics of the simulation series exploring the effect of non-ideal MHD effects by comparing Models 0 (fiducial) and I (ideal MHD), showing the kinetic energy spectra (top panel; an $E(k) \propto k^{-2}$ line is also presented for reference), $\lg T$ distributions (middle panel), and $\lg \rho$ distributions (lower panel).

ing causes a continuous drop in gas temperature over the following 10^6 yr.

4.2. Turbulence Energy Injection

Turbulent energy injection (see §2.3) is the ultimate energy source in all simulations throughout this paper. By turning the knob that controls the injection rate $\dot{\epsilon}_{\text{turb}}$ in Models T2 and T4 (injection rates 3×10^{-2} and 3×10^{-4} in units $\text{erg g}^{-1} \text{s}^{-1}$, respectively), the turbulence cascade and almost all phenomena attached to it will experience considerable changes constrained by their energy budgets.

The most prominent consequence of ϵ_{turb} is the distribution of gas dynamics and thermodynamics. Figure 11

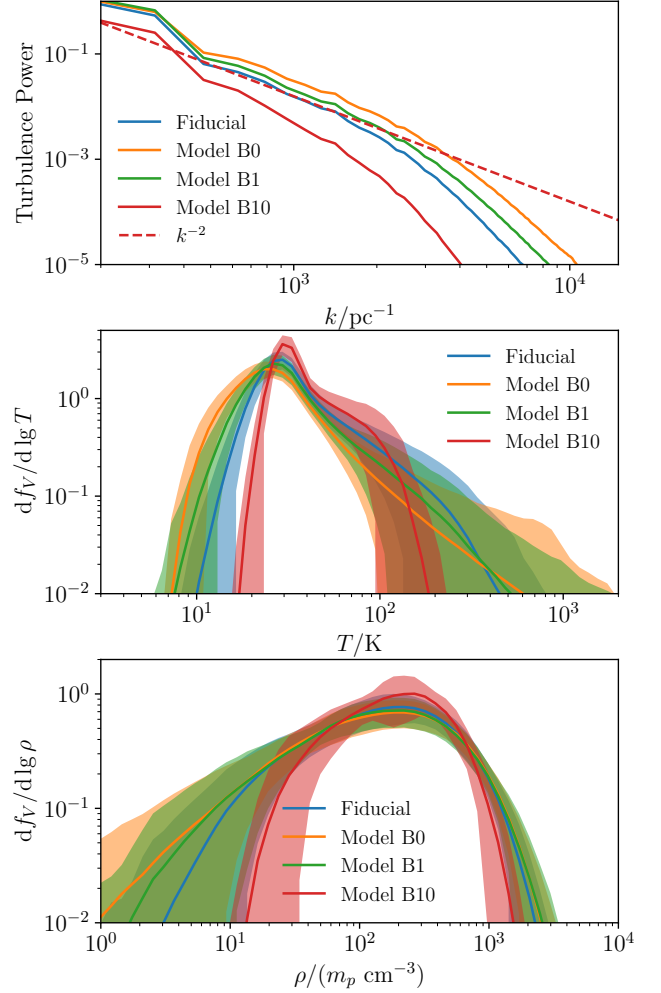


Figure 9. Similar to Figure 8 but for the series with different initial magnetic field strengths (Models 0, B0, B1, and B10).

compares Models T2 and T4 with the fiducial Model 0 for their statistical functions. The shapes of the kinetic energy spectra are almost identical at wavenumbers below the damping wavenumber $k \simeq 1.5 \times 10^3 \text{ pc}^{-1}$, while the amplitude grows sublinearly with increasing intensity of turbulence energy cascades. Above that wave number, the cases with stronger energy injection are relatively less susceptible to the inhibition of the kinetic power by the damping mechanisms including magnetic fields and diffusivities on smaller spatial scales, and vice versa.

The density and temperature distributions in this series exhibit a clear trend that higher $\dot{\epsilon}_{\text{turb}}$ leads to “broader” distributions in both $\lg T$ and $\lg \rho$ space by allowing for more vigorous shocks, compressions, and adiabatic expansions. This fact suggests a promising way to quantify the turbulence energy crossing rates

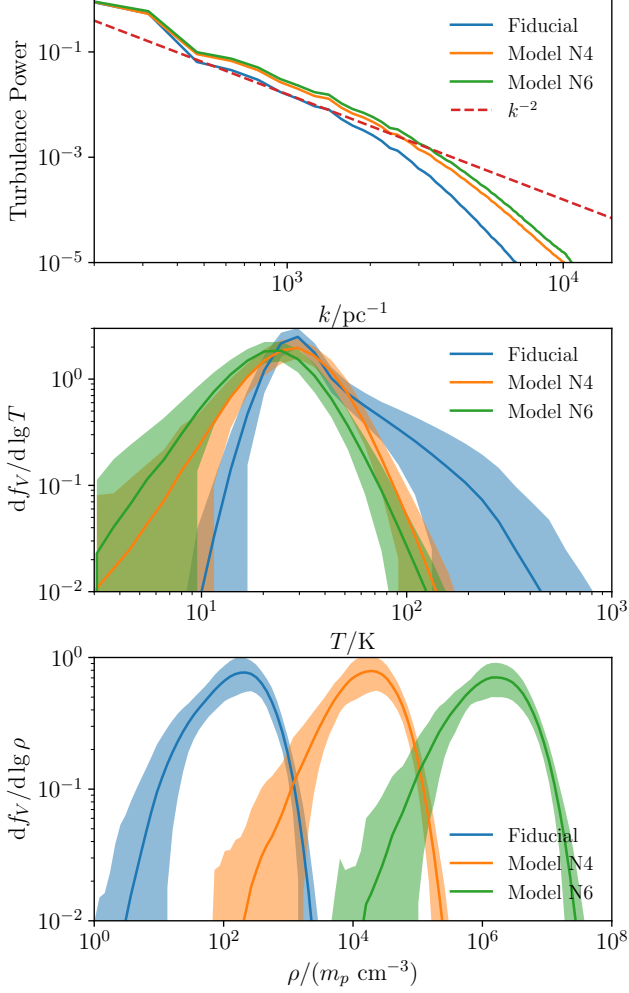


Figure 10. Similar to Figure 8 but for the series with different average mass densities (Models 0, N4 and N6).

via the measurements of temperature and density distributions of concerned molecular gases. For instance, the temperature distributions are reasonably sensitive to $\dot{\epsilon}_{\text{turb}}$, as Model T4 exhibits little gas warmer than ~ 60 K, while Model T2 has a non-negligible fraction with $T \gtrsim 10^3$ K. Admittedly, multiple other factors affect gas temperature distributions, causing parametric degeneracies. Therefore, quantitative measurement of the turbulence power relies on other constraints, e.g., the abundance of OH is positively correlated to $\dot{\epsilon}_{\text{turb}}$ (Table 2), due to the enhanced reaction rates at higher density and temperatures. Synthetic mock observations are necessary in the following works to confront the simulation results directly with observations.

4.3. Thermochemical Conditions

There are two major ionization channels in the simulation: (a) ISRF ionization of carbon and (b) cosmic

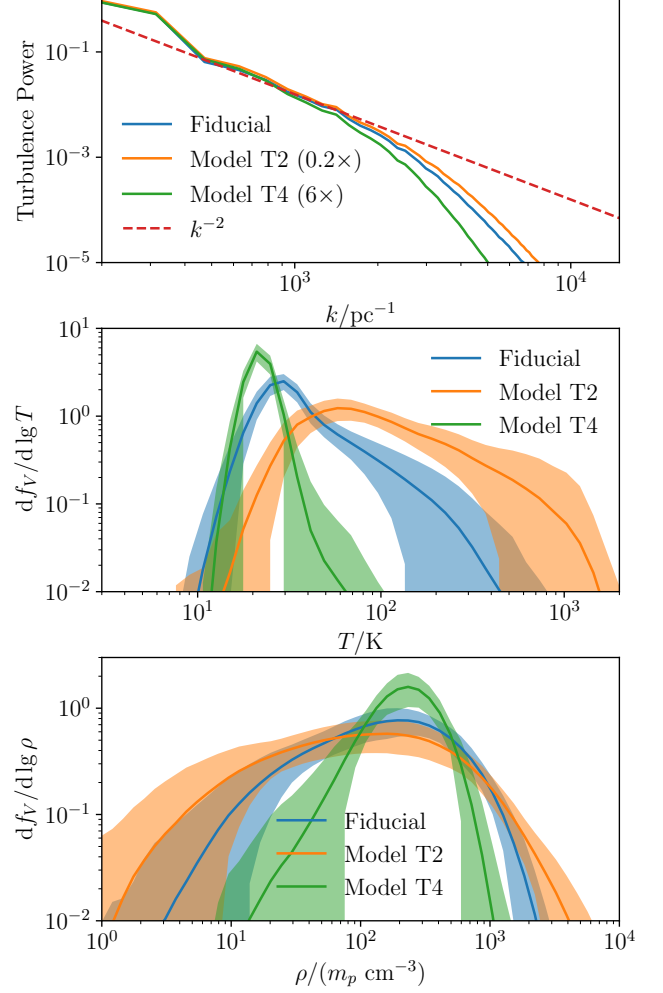


Figure 11. Similar to Figure 8 but for the series with different turbulence energy injection rates (Models 0, T2, and T4). Note that the power spectra for T2 and T4 have adjusted by scaling factors (indicated in the legend), so that their spectra on the lowest wavenumbers overlap for better comparison.

ray ionization (mainly on H_2 , H and He). These processes not only provide necessary coupling between gas and fields but also effectively initiate the formation of relevant chemical species, including C^+ , CO, OH, which are the most important ones in terms of the gas thermodynamics.

The statistics of simulations have revealed that the kinetic energy spectra and the $\lg \rho$ distribution functions of these models are affected only very slightly. Therefore, Figure 12 only emphasizes the comparisons in the $\lg T$ space. Model G3 has a relatively similar $\lg T$ distribution function compared to Model 0, with the lower end slightly warmer due to the increased ISRF destruction of molecular coolants (CO and OH). Model G0, with the

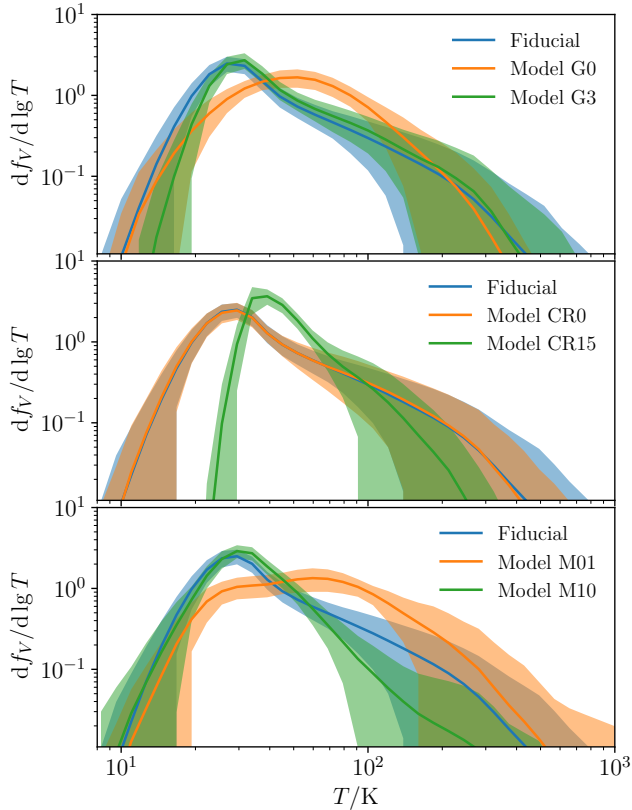


Figure 12. Similar to the middle panel of Figure 8, with models varying the cosmic ray intensities (left column; Models 0, CR0, and CR15), and the ISRF (right column; Models 0, G0, and G3). The power spectra and $\lg \rho$ distributions are omitted as they are very similar to the fiducial model.

lack of production in the most critical coolants C^+ and CO , exhibits a $\lg T$ profile that mostly fits the standard log-normal distribution. With excessive cosmic ray ionization, Model CR15 has a $\sim 2.5\times$ higher cutoff on the low-temperature end due to extra cosmic ray heating, while its high end of $\lg T$ distribution is qualitatively similar to Model I due to higher abundances of charge carriers and tighter fluid-field couplings. Since the most important coolants are often metal-related, altering the gas’s metallicity impacts the gas temperatures. Models 0, M01, and M10 have almost the same lower limit in the temperature distribution functions (approximately $T \sim 10$ K), while their high ends are anti-correlated with the metallicity. In brief, the thermodynamic conditions can provide specific constraints on the properties of the irradiation and cooling processes in molecular gases.

5. DISCUSSIONS AND SUMMARY

In this work, we have studied the characteristics and evolution of diffuse ($\rho \sim 250 m_p \text{ cm}^{-3}$), magnetized ($B_0 = 3 \mu G$) molecular clouds, using MHD simula-

tions co-evolved with consistent non-equilibrium thermochemistry. Although mostly numerical and theoretical, these simulations have revealed prospective clues that can play crucial roles in constraining diffuse molecular gas properties via observational measurements.

5.1. Fields, Fluids, and their Interactions

Co-evolved with thermochemistry, we observe from the simulation models that the behaviors of gas dynamics are predominantly controlled by the turbulence and MHD properties themselves. The $\lg T$ distributions (especially their high-temperature cutoff) are hopefully the most sensitive indicator of the turbulence energy injection rate. With consistent thermochemistry considered, the thermal energy budgets at quasi-steady states are mostly balanced, and the temperature profiles will reveal the dynamics relatively robustly. The $\lg T$ profiles are susceptible to other factors, including total densities, ionizing radiations (and cosmic rays), field intensities, and metallicities. Nevertheless, as discussed in §4, these factors only affect $\lg T$ with secondary importance, especially regarding the high-temperature cutoffs in these diffuse molecular gases. In observations aiming at constraining the gas dynamic properties, various nebula diagnostics can determine the gas temperature distribution in interested regions and constrain the turbulence energy injections with relatively high confidence.

The field strengths we have studied are marginally crucial in curbing the formation of turbulence structures, except for Model B10, whose average plasma $\beta \lesssim 10^{-1}$ causes significant inhibition of turbulent structure growths. The simulated models are mostly weakly ionized, and non-ideal MHD is desired to model the kinematics and dynamics. Due to magnetic diffusions, hydrodynamic profiles are not very sensitive probes in the fields. However, the upper limit of fields can still be constrained by the temperature assisted with other measurements.

5.2. The Necessity of Non-ideal MHD Studies with Consistent Thermochemistry

5.2.1. Magnetic Fields

There have been many recent numerical simulations aiming at the turbulence dynamics within the interstellar medium (ISM), including the behavior within molecular clouds. A prime example is the work by Federath et al. (2021), which achieved remarkable resolution through hydrodynamic simulations, albeit without incorporating magnetic fields. One of the major conclusions of this study is the crucial role that magnetic fields play in sculpting the turbulence power spectra, especially the damping wavenumber. The magnetic pres-

sure and tension are found to impede the development of structures at smaller scales. In scenarios devoid of magnetic fields, the energy cascade is observed to extend to the highest attainable wavenumbers, constrained only by numerical dissipations at the resolution limits. However, this overlooks the actual spatial scales at which damping occurs, given that magnetization is a pervasive characteristic of the ISM under consideration. This oversight underscores the necessity for simulations to account for the influence of magnetic fields to more accurately reflect the ISM’s behavior.

5.2.2. Magnetic Diffusivities

Even the simulations incorporating MHD, such as Ostriker et al. (1999); Porter et al. (2015); Bian & Aluie (2019); Grete et al. (2021), often overlook a critical aspect: the influence of non-ideal MHD effects. As depicted in Figure 4 and corroborated by numerous other simulations, regions that are susceptible to non-ideal MHD effects (indicated by Re_p at the order of unity) constitute a significant portion of the simulated volume, particularly at the peripheries of compressed gas clumps. This phenomenon specifically impacts the morphology at smaller scales, as illustrated by the comparison between Model 0 and Model I in Figure 8. The damping scale, influenced by magnetic diffusivities, is approximately twice as extensive as in scenarios modeled with ideal MHD, where the effective magnetic diffusivities are numerical artifacts contingent on resolution.

Also elaborated by Grete et al. (2023), the dissipation scales in MHD play a pivotal role in determining how magnetic fields sculpt the dynamics of the gas. The accurate incorporation of magnetic diffusivities in simulations that resolve the spatial scales of diffusion is essential to circumvent such artifacts. Moreover, magnetic diffusivities are sensitively dependent on the actual thermochemical conditions of the gas, including the concentration and types of charge carriers, the densities of neutral gas, and the prevailing temperatures. These physical variables are contingent on the evolutionary history of the gases and should not be reduced to mere status variables. Consequently, non-ideal MHD simulations of molecular gases that employ prescribed parametrization of diffusivities or highly simplified chemical networks, as seen in Downes & O’Sullivan (2009); Tilley & Balsara (2011); Jones & Downes (2011, 2012); Wurster et al. (2016), inevitably sacrifice consistency. This is due to the fact that many reactions related to ionization, recombination, and charge transfer involve complex molecular and ionic species, and sometimes even surface chemical processes. This realization has already been acknowledged in studies of protoplanetary disks

(e.g., Bai & Goodman 2009; Xu & Bai 2016; Wang et al. 2019) and has been identified as being equally significant for the diffuse molecular gases discussed in this paper, as exemplified in Figure 12.

5.2.3. Equation of State and Thermodynamics

The majority of prior research works, either with hydrodynamics or MHD, have employed an isothermal equation of state (EoS), neglecting the essential dissipation mechanisms carried out by comprehensive thermochemical approaches. It is acknowledged that simulations relying solely on an adiabatic EoS in the absence of cooling will eventually convert all injected energy into thermal energy of the gas, overwhelming the kinetic and magnetic energy and finally smearing out the turbulent structures. However, the use of an isothermal EoS as a simplification also significantly compromises physical fidelity.

Consider the scenario of a gas clump that undergoes rapid compression prior to cooling. The gas pressure, and consequently its internal energy density, scales with the length scale l of the clump as $p \propto l^{-3\gamma}$, while the density scales as $\rho \propto l^{-3}$. The cooling rate per unit volume at a constant temperature is proportional to $\Lambda\rho^2 \propto l^{-6}$, a steeper power-law than that of the gas pressure. This indicates that the compressed gas patch will undergo runaway cooling until it reaches a significantly lower temperature, at which Λ almost diminishes compared to its ambient value (for molecular gas, this temperature is typically around ~ 10 K), while other regions of the gas remain at higher temperatures. This phenomenon results in a broad temperature distribution that spans several orders of magnitude, as observable in e.g., Figures 4 and Section 4.

The presence of a broad temperature distribution within turbulent materials is essential for interpreting the diagnostics of observed nebulae. For instance, the work by Goldsmith et al. (2010) has already identified the emission of rotational transitions of H_2 from diffuse molecular regions with a median temperature $\lesssim 50$ K. This finding underscores the importance of regions heated to temperatures above $\gtrsim 10^2$ K through gas dynamics, thereby highlighting the need for consistent thermodynamics in ISM simulations. In contrast, the simplified dichotomy of “supersonic versus subsonic scales” as emphasized in isothermal simulations, including those by Federrath et al. (2021), does not accurately reflect the complexities of astrophysical phenomena taking place in the diffuse molecular gas.

When aligning simulation results with ISM observations, the acquisition of consistent temperature profiles is imperative for the precise interpretation of spectral di-

agnostics pertaining to the properties of the gas. These considerations underscore the necessity for the integration of robust thermochemical computations within simulation models, moving beyond the limitations of the overly simplified isothermal equation of state. This approach is vital for capturing the nuanced interplay of physical processes that govern the behavior of the interstellar medium.

5.2.4. *Dimensionless versus Dimensional*

Most of the simulations on turbulent ISM follow the dimensionless approach. When the final dissipation is based on realistic microphysical mechanisms (including magnetic diffusion, radiative cooling, etc.) rather than mathematical or numerical dissipations, one can easily confirm with basic dimensional analyses that the microphysical processes cannot be non-dimensionalized simultaneously with the hydrodynamics or MHD. This fact inevitably add to the complications and computational costs, yet this is the inevitable costs that one has to pay to understand turbulent gases that are coupled with physical mechanisms that are crucial to the ultimate dissipation along the turbulence energy cascade, including magnetic fields and multi-scale physics.

5.3. *Thermochemical Probes of Diffuse Molecular Gases*

Given relatively strong turbulence driving processes, constraining thermochemistry via dynamic profiles are indirect and may suffer from degeneracies of parameters—probably except for the influence by metallicities on the higher limits of temperatures, which can be constrained in conjunction with the specific turbulence powers via the upper limits in T . Instead, thermochemistry itself is the probe of multiple dynamical processes. This probe can only be forged with turbulent ISM simulations that can directly yield analyses consistently with real-time thermochemistry. Adopting isothermal EoS may mislead the interactions connecting the gas dynamics to chemistry and subsequent observables, by providing inconsistent key parameters including compression ratios and temperatures.

One prospectively interesting indicator that deserves extra effort is the CO relative abundances, X_{CO} . Presumably, this is mostly a constant used to infer total gas densities in many studies, yet our simulations suggest that X_{CO} varies from place to place, from time to time. The conversion from C^+ to CO takes $\sim 2 \times 10^5$ yr to equilibrate the photodissociation. Before that, the reduced CO relative abundance could be a helpful indicator limiting the evolution history of the gas. This constraint should be confirmed with the measurement of C^+ and CH, which are essential materials and intermediate products in the reaction chains for CO formation.

Another promising probe is OH, which is a sharp indication of cosmic ionization of H_2 (and atomic O as well, with roughly half of the importance in the chemical network). Due to similar ionization energy values for hydrogen and oxygen, efficient ionization can only come from high-penetration sources, including the cosmic ray or the external X-ray irradiation from, e.g., young protostars (not included in this paper). Since the relative abundance of OH keeps climbing throughout the $\sim 2 \times 10^5$ yr period at the beginning of evolution, the measurements could also help constrain the age of the system. The reaction $\text{H}_2\text{O}^+ + \text{H}_2 \rightarrow \text{H}_3\text{O}^+ + \text{H}$, one of the slowest steps in the OH formation chain in such weakly ionized media, is insensitive to temperature. In the meantime, the photodissociation of OH is another limiting factor, as the process relies on the strong electric dipole and is not susceptible to self or cross-shielding. Both factors make the final product OH a possible indication of a few physical parameters, including local density and the ISRF intensity. Consistent interpretations of observations will require simulations for reasonable fittings on the measurement results.

5.4. *Future Works*

Our current work focuses on numerical simulations, their intrinsic MHD processes, and the properties based on the interactions between MHD, radiation (ISRF and cosmic ray), and thermochemistry. In future works, we will elaborate on possible predictions by synthesizing mock observations. One possibility is the line intensities, either spatially resolved or integrated. Combined with consistent MHD and thermodynamics, the spatial distribution features of physical diffuse molecular cloud models can be converted into expectations on actual astronomical measurements. Another possibility is the distribution profiles in the position-position and position-position-velocity (PPV) spaces. By confronting observables with synthetic profiles generated from an adequate number of simulations, plausible interpretations of measurements will be achieved via searching the parameter space, supported by proper microphysical details that interact consistently with the dynamics and their observational tracers.

N. Yue, L. Wang, T. Bisbas, and D. Quan are funded by Zhejiang Laboratory Scientific Project # K2022PE0AB01. We also acknowledge the computing resources provided by the Kavli Institute for Astronomy and Astrophysics in Peking University. We thank our colleagues for helpful discussions: Paul Goldsmith, Xin Wang, and Haifeng Yang.

REFERENCES

- Bai, X.-N. 2011, *ApJ*, 739, 51,
doi: [10.1088/0004-637X/739/1/51](https://doi.org/10.1088/0004-637X/739/1/51)
- Bai, X.-N., & Goodman, J. 2009, *ApJ*, 701, 737
- Bian, X., & Aluie, H. 2019, *PhRvL*, 122, 135101,
doi: [10.1103/PhysRevLett.122.135101](https://doi.org/10.1103/PhysRevLett.122.135101)
- Boldyrev, S., & Perez, J. C. 2009, *PhRvL*, 103, 225001,
doi: [10.1103/PhysRevLett.103.225001](https://doi.org/10.1103/PhysRevLett.103.225001)
- Cazaux, S., Martín-Doménech, R., Chen, Y. J., Muñoz Caro, G. M., & González Díaz, C. 2017, *ApJ*, 849, 80,
doi: [10.3847/1538-4357/aa8b0c](https://doi.org/10.3847/1538-4357/aa8b0c)
- Clark, P. C., Glover, S. C. O., Ragan, S. E., & Duarte-Cabral, A. 2019, *MNRAS*, 486, 4622,
doi: [10.1093/mnras/stz1119](https://doi.org/10.1093/mnras/stz1119)
- Downes, T. P., & O’Sullivan, S. 2009, *ApJ*, 701, 1258,
doi: [10.1088/0004-637X/701/2/1258](https://doi.org/10.1088/0004-637X/701/2/1258)
- Draine, B. T. 2011, *Physics of the Interstellar and Intergalactic Medium* (Princeton University Press)
- Draine, B. T., & Bertoldi, F. 1996, *ApJ*, 468, 269,
doi: [10.1086/177689](https://doi.org/10.1086/177689)
- Federrath, C., Klessen, R. S., Iapichino, L., & Beattie, J. R. 2021, *Nature Astronomy*, 5, 365,
doi: [10.1038/s41550-020-01282-z](https://doi.org/10.1038/s41550-020-01282-z)
- Franeck, A., Walch, S., Seifried, D., et al. 2018, *MNRAS*, 481, 4277, doi: [10.1093/mnras/sty2507](https://doi.org/10.1093/mnras/sty2507)
- Glover, S. C. O., & Jappsen, A. K. 2007, *ApJ*, 666, 1,
doi: [10.1086/519445](https://doi.org/10.1086/519445)
- Goldsmith, P. F., Velusamy, T., Li, D., & Langer, W. D. 2010, *ApJ*, 715, 1370,
doi: [10.1088/0004-637X/715/2/1370](https://doi.org/10.1088/0004-637X/715/2/1370)
- Grete, P., O’Shea, B. W., & Beckwith, K. 2021, *ApJ*, 909, 148, doi: [10.3847/1538-4357/abdd22](https://doi.org/10.3847/1538-4357/abdd22)
- . 2023, *ApJL*, 942, L34, doi: [10.3847/2041-8213/acaea7](https://doi.org/10.3847/2041-8213/acaea7)
- Heays, A. N., Bosman, A. D., & van Dishoeck, E. F. 2017, *A&A*, 602, A105, doi: [10.1051/0004-6361/201628742](https://doi.org/10.1051/0004-6361/201628742)
- Hennelbelle, P., & Falgarone, E. 2012, *A&A Rv*, 20, 55,
doi: [10.1007/s00159-012-0055-y](https://doi.org/10.1007/s00159-012-0055-y)
- Ingalls, J. G., Bania, T. M., Boulanger, F., et al. 2011, *ApJ*, 743, 174, doi: [10.1088/0004-637X/743/2/174](https://doi.org/10.1088/0004-637X/743/2/174)
- Jappsen, A. K., Glover, S. C. O., Klessen, R. S., & Mac Low, M. M. 2007, *ApJ*, 660, 1332, doi: [10.1086/513085](https://doi.org/10.1086/513085)
- Jones, A. C., & Downes, T. P. 2011, *MNRAS*, 418, 390,
doi: [10.1111/j.1365-2966.2011.19491.x](https://doi.org/10.1111/j.1365-2966.2011.19491.x)
- . 2012, *MNRAS*, 420, 817,
doi: [10.1111/j.1365-2966.2011.20095.x](https://doi.org/10.1111/j.1365-2966.2011.20095.x)
- Kim, J.-G., Kim, W.-T., & Ostriker, E. C. 2018, *ApJ*, 859, 68, doi: [10.3847/1538-4357/aabe27](https://doi.org/10.3847/1538-4357/aabe27)
- . 2019, *ApJ*, 883, 102, doi: [10.3847/1538-4357/ab3d3d](https://doi.org/10.3847/1538-4357/ab3d3d)
- Kowal, G., Lazarian, A., & Beresnyak, A. 2007, *ApJ*, 658, 423, doi: [10.1086/511515](https://doi.org/10.1086/511515)
- Langer, W. D., Velusamy, T., Pineda, J. L., et al. 2010, *A&A*, 521, L17, doi: [10.1051/0004-6361/201015088](https://doi.org/10.1051/0004-6361/201015088)
- Lupi, A., Bovino, S., & Grassi, T. 2021, *A&A*, 654, L6,
doi: [10.1051/0004-6361/202142145](https://doi.org/10.1051/0004-6361/202142145)
- Mac Low, M.-M. 1999, *ApJ*, 524, 169, doi: [10.1086/307784](https://doi.org/10.1086/307784)
- Mac Low, M.-M., Klessen, R. S., Burkert, A., & Smith, M. D. 1998, *PhRvL*, 80, 2754,
doi: [10.1103/PhysRevLett.80.2754](https://doi.org/10.1103/PhysRevLett.80.2754)
- McElroy, D., Walsh, C., Markwick, A. J., et al. 2013, *A&A*, 550, A36
- McKee, C. F., & Ostriker, E. C. 2007, *ARA&A*, 45, 565,
doi: [10.1146/annurev.astro.45.051806.110602](https://doi.org/10.1146/annurev.astro.45.051806.110602)
- Nehmé, C., Gry, C., Boulanger, F., et al. 2008, *A&A*, 483, 471, doi: [10.1051/0004-6361:20078373](https://doi.org/10.1051/0004-6361:20078373)
- Neufeld, D. A., & Kaufman, M. J. 1993, *ApJ*, 418, 263,
doi: [10.1086/173388](https://doi.org/10.1086/173388)
- Neufeld, D. A., Lepp, S., & Melnick, G. J. 1995, *ApJS*, 100, 132, doi: [10.1086/192211](https://doi.org/10.1086/192211)
- Omukai, K., Hosokawa, T., & Yoshida, N. 2010, *ApJ*, 722, 1793, doi: [10.1088/0004-637X/722/2/1793](https://doi.org/10.1088/0004-637X/722/2/1793)
- Ostriker, E. C., Gammie, C. F., & Stone, J. M. 1999, *ApJ*, 513, 259, doi: [10.1086/306842](https://doi.org/10.1086/306842)
- Pantaleone, S., Enrique-Romero, J., Ceccarelli, C., et al. 2021, *ApJ*, 917, 49, doi: [10.3847/1538-4357/ac0142](https://doi.org/10.3847/1538-4357/ac0142)
- Pineda, J. L., Velusamy, T., Langer, W. D., et al. 2010, *A&A*, 521, L19, doi: [10.1051/0004-6361/201015089](https://doi.org/10.1051/0004-6361/201015089)
- Porter, D. H., Jones, T. W., & Ryu, D. 2015, *ApJ*, 810, 93,
doi: [10.1088/0004-637X/810/2/93](https://doi.org/10.1088/0004-637X/810/2/93)
- Qian, L., Li, D., Gao, Y., Xu, H., & Pan, Z. 2018, *ApJ*, 864, 116, doi: [10.3847/1538-4357/aad780](https://doi.org/10.3847/1538-4357/aad780)
- Raskutti, S., Ostriker, E. C., & Skinner, M. A. 2016, *ApJ*, 829, 130, doi: [10.3847/0004-637X/829/2/130](https://doi.org/10.3847/0004-637X/829/2/130)
- . 2017, *ApJ*, 850, 112, doi: [10.3847/1538-4357/aa965e](https://doi.org/10.3847/1538-4357/aa965e)
- Rice, J. S., Federman, S. R., Flagey, N., et al. 2018, *ApJ*, 858, 111, doi: [10.3847/1538-4357/aabae7](https://doi.org/10.3847/1538-4357/aabae7)
- Richings, A. J., Schaye, J., & Oppenheimer, B. D. 2014a, *MNRAS*, 440, 3349, doi: [10.1093/mnras/stu525](https://doi.org/10.1093/mnras/stu525)
- . 2014b, *MNRAS*, 442, 2780, doi: [10.1093/mnras/stu1046](https://doi.org/10.1093/mnras/stu1046)
- Stone, J. M., Tomida, K., White, C. J., & Felker, K. G. 2020, *ApJS*, 249, 4, doi: [10.3847/1538-4365/ab929b](https://doi.org/10.3847/1538-4365/ab929b)
- Tilley, D. A., & Balsara, D. S. 2011, *MNRAS*, 415, 3681,
doi: [10.1111/j.1365-2966.2011.18982.x](https://doi.org/10.1111/j.1365-2966.2011.18982.x)
- Wang, L., Bai, X.-N., & Goodman, J. 2019, *ApJ*, 874, 90,
doi: [10.3847/1538-4357/ab06fd](https://doi.org/10.3847/1538-4357/ab06fd)
- Wang, L., & Dai, F. 2021, *ApJ*, 914, 98,
doi: [10.3847/1538-4357/abflee](https://doi.org/10.3847/1538-4357/abflee)
- Wang, L., & Goodman, J. 2017, *ApJ*, 847, 11,
<http://stacks.iop.org/0004-637X/847/i=1/a=11>

- Whitworth, A. P., & Jaffa, S. E. 2018, *A&A*, 611, A20,
doi: [10.1051/0004-6361/201731871](https://doi.org/10.1051/0004-6361/201731871)
- Wurster, J., Bate, M. R., & Price, D. J. 2019, *MNRAS*,
489, 1719, doi: [10.1093/mnras/stz2215](https://doi.org/10.1093/mnras/stz2215)
- Wurster, J., Price, D. J., & Bate, M. R. 2016, *MNRAS*,
457, 1037, doi: [10.1093/mnras/stw013](https://doi.org/10.1093/mnras/stw013)

- Wurster, J., & Rowan, C. 2024, *MNRAS*, 528, 2257,
doi: [10.1093/mnras/stae090](https://doi.org/10.1093/mnras/stae090)
- Xu, R., & Bai, X.-N. 2016, *ApJ*, 819, 68,
doi: [10.3847/0004-637X/819/1/68](https://doi.org/10.3847/0004-637X/819/1/68)

APPENDIX

A. HYDROSTATIC MODELS

Figure 13 presents the two tests’ most abundant and essential chemical species. These test runs are identical to the fiducial model except that they are static (i.e., have *no* turbulence injection), and one of them has zero cosmic ray intensity as well (the lower panel). In order to verify that our simulation system—already verified in various non-ideal MHD simulations for PPDs and planetary atmospheres—is also functioning correctly for the diffuse molecular clouds, this appendix elaborates on the consistency of a few key species by comparing the simulated key values of chemical kinetics with analytic results.

We first examine the species related to hydrogen. Both models exhibit the dissociation of hydrogen molecules over the 10^6 yr evolution, at the end of which the abundance of atomic H reaches $\sim 10^{-2}$ due to the photodissociation by the ISRF. As the self-shielding of H_2 is considered with the effective shielding length $l_{\text{cap}} \sim 1$ pc on a uniform medium (see also §2.2) with $\rho = 250 m_p \text{ cm}^{-3}$ (or $n(H_2) \simeq 200 \text{ cm}^{-3}$) and $T = 30$ K, one gets the self-shielding factor $f_{H_2} \simeq 2.5 \times 10^{-5}$ using the recipes in [Draine & Bertoldi \(1996\)](#). This leads to a $\zeta_{\text{diss}, H_2} \simeq 3 \times 10^{-16} \text{ s}^{-1}$ photodissociation rate, yielding $n(H) \simeq 1.9 \text{ cm}^{-3} \simeq 10^{-2} n_H$. The free electrons are predominantly provided by the ISRF ionization of C, whose abundance almost equals the elemental abundance of carbon. The H^+ concentration is eliminated by the radiative recombination (whose rate coefficient is $\alpha_H \simeq 2 \times 10^{-11} \text{ cm}^3 \text{ s}^{-1}$ at 30 K) at the timescale $\tau_{H^+} = (n_e \alpha_H)^{-1} \simeq 4.6 \times 10^4 \text{ yr}$, in the absence of cosmic rays. With $\zeta_{\text{CR}} = 10^{-17} \text{ s}^{-1}$, radiative recombination maintains $n(H^+) \simeq n_H \zeta_{\text{CR}} \tau_{H^+} \simeq 1.2 \times 10^{-3} \text{ cm}^{-3}$. These results agree quantitatively with the test models.

The formation of CO follows a chain of reactions from C^+ to CH (see e.g., [Draine 2011](#)), starting from $C^+ + H_2 \rightarrow CH_2^+$. At 30 K and the 1 abundances, this reaction has a $\sim 4.6 \times 10^{-15} \text{ cm}^{-3} \text{ s}^{-1}$ production rate of CH_2^+ , a quarter of which is instantly converted to CH by dissociative recombination with e^- (equivalent to a CH production rate of $\sim 1.2 \times 10^{-15} \text{ cm}^{-3} \text{ s}^{-1}$). The final step $CH + O \rightarrow CO + H$ competes with $CH + H \rightarrow C + H_2$. The sum of these two reactions consume CH at the timescales $\tau_{\text{CH}} \sim 1.3 \times 10^{11} \text{ s}$, constraining the CH abundance to be $n(\text{CH}) \simeq 1.6 \times 10^{-4} \text{ cm}^{-3}$, and leading to a production rate of CO of $\sim 6 \times 10^{-16} \text{ cm}^{-3} \text{ s}^{-1}$. Consider the ISRF photodissociation rate $\zeta_{\text{CO}} \simeq 4 \times 10^{-11} \text{ s}^{-1}$ (with $0.3 G_0$ and the total shielding factor ~ 0.57 es-

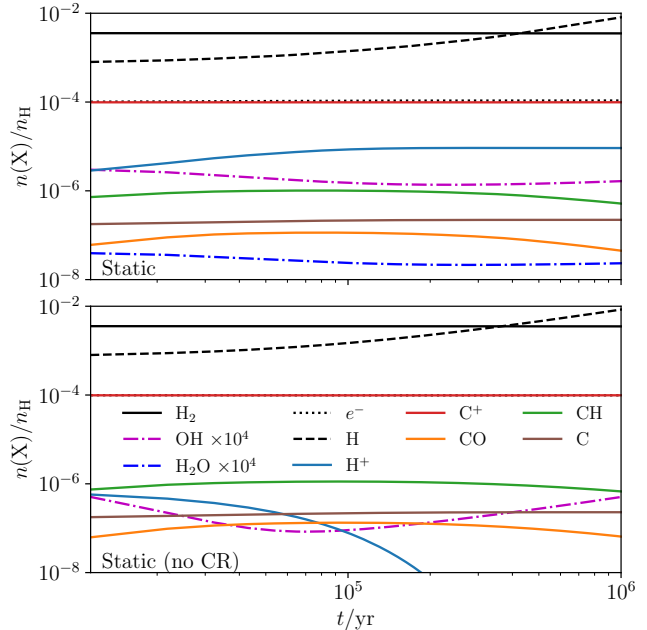


Figure 13. Similar to the Panel (b) of Figure 1 but for the two test simulation models under hydrostatics (viz. no turbulences or any kinematics). The two panels present the results with and without cosmic rays, respectively.

timated using the recipes in [Heays et al. 2017](#)), such CO production rate leads to $n(\text{CO}) \simeq 1.5 \times 10^{-5} \text{ cm}^{-3}$. The slight drop of CO abundance since $t \sim 10^5$ yr is attributed to the increase of atomic H. In addition to confirming species abundances with Figure 13, we also verify that the analytic estimates of reaction rates are quantitatively consistent with the outputs given by the test simulations (not shown in the figures).